Hyper-reduced order models for accelerating parametric analyses on reinforced concrete structures subjected to earthquakes

Bastien Bodnar, Walid Larbi, Magdalini Titirla, Jean-François Deü, Fabrice Gatuingt, Frédéric Ragueneau

Received: 26 April 2023 | Accepted: 23 October 2023

DOI: 10.1111/mice.13120

COMPUTER-AIDED CIVIL AND INFRASTRUCTURE ENGINEERING WILEY

RESEARCH ARTICLE

Hyper-reduced order models for accelerating parametric analyses on reinforced concrete structures subjected to earthquakes

Bastien Bodnar[1,2] | **Walid Larbi**[1] | **Magdalini Titirla**[1] | **Jean-François Deü**[1] | **Fabrice Gatuingt**[2] | **Frédéric Ragueneau**[2,3]

[1]Laboratoire de Mécanique des Structures et des Systèmes Couplés, Conservatoire National des Arts et Métiers, Paris, France

[2]Laboratoire de Mécanique Paris-Saclay, Université Paris-Saclay, Centrale Supélec, ENS Paris-Saclay, CNRS, Gif-sur-Yvette, France

[3]EPF École d'Ingénieurs, Cachan, France

Correspondence
Fabrice Gatuingt, Laboratoire de Mecanique Paris-Saclay, Universite Paris-Saclay, Centrale Supelec, ENS Paris-Saclay, CNRS, 4 avenue des Sciences, 91190 Gif-sur- Yvette, France.
Email: fabrice.gatuingt@ens-paris-saclay.fr

Abstract

This paper combines a hyper-reduction procedure, the proper orthogonal decomposition unassembled discrete empirical interpolation method, with a non-iterative α-operator splitting (α-OS) time-integration scheme for accelerating parametric analyses on damageable civil engineering structures subjected to earthquakes. Applications on a two-story reinforced concrete frame building modeled by multi-fiber beams provide guidelines to define hyper-reduced order models (HROMs) for real-life applications that use seismic databases or variable loading assumptions. The α-OS HROMs proved their applicability in approximating high-fidelity dynamic responses with speed-up factors higher than 60 and errors lower than 0.6% for the present case study.

1 | INTRODUCTION

An important part of civil engineering structures design is the capability to withstand earthquakes. The variability of seismic loadings requires multiple reassessments of the structural responses to efficiently optimize the construction costs (Sarma & Adeli, 1998). Classical simplified approaches, such as lateral forces, spectral, modal, push-over, or linear dynamic analyses can be used to evaluate the response of civil engineering structures (Chopra, 2017), whose design should meet all the safety requirements (e.g., horizontal drift, seismic force, or seismic demand) specified by the building codes. All these methods are very efficient and widely used in design offices for structural optimization but remain limited, compared to nonlinear dynamic analyses since most of them do not capture all the physics of the actual dynamic responses (e.g., kinematics, loading path-dependent dissipative mechanisms, or torsion at floor level).

As earthquakes are critical loadings, performing tridimensional (3D) nonlinear dynamic analyses helps model the damage growth physically. If beam elements are commonly used with plastic hinges to model frame structures (Hafezolghorani et al., 2022), meshes that include local or semi-global damageable finite elements (e.g., multi-fiber beams or multilayer shells) allow for precisely modeling complex dissipative mechanisms (e.g., damage, frictional sliding, or kinematic hardening) that appear at local scale over the height and the width of sections or at column/beam connections (Hervé-Secourgeon, 2021).

Combining such models with kriging methods (Yuan et al., 2023), machine learning algorithms, or neural networks to build response surfaces could significantly improve the existing optimization and structural

monitoring methods. Modal and push-over analyses are already used with machine learning algorithms that are supplied by measured data for damage detection (Ozdaghli & Koutsoukos, 2019; Wen et al., 2023) and structural health monitoring (Hwang et al., 2022). Structures can also be efficiently optimized with linear analyses involving stochastic dynamic loadings (Xu et al., 2017) or parametric analyses on nonlinear simplified macro elements using neural networks (Noureldin et al., 2023). As an extension of the above-mentioned methods, nonlinear dynamic analyses on high-dimensional systems could be coupled with interpolation methods (e.g., kriging) to build complex parametric response surfaces for models defined by loading path-dependent variables (e.g., damage index or accumulated plastic strain). However, this dependency requires using local material laws (e.g., quasi-brittle softening damage laws for concrete), which increases the central processing unit (CPU) time that is needed to update the material properties when the nonlinear Finite Element dynamic analyses proceed, in particular for high-dimensional systems.

Efficient algorithms are required to solve such problems (Adeli et al., 1978), with an optimized implementation in accordance with the computer system architecture (Adeli & Yu, 1995; Yu & Adeli, 1993). However, as parametric response surfaces require a huge number of data to be correctly defined, a special treatment still needs to be applied to reduce the computational cost of the nonlinear analyses used to define reference solutions for the interpolation algorithms.

As high-dimensional systems require more random access memory (RAM) to be solved, reducing their size is necessary. An efficient way to accelerate the computation of the structural responses consists of using available high-order solutions to approximate new ones on a reduced basis. Such reduced order modeling (ROM) procedures could be used with the above-mentioned methods (e.g., machine learning, neural networks, or kriging) to efficiently build response surfaces for complex nonlinear parametric systems.

Craig and Bampton (1968) were the first to propose an efficient ROM method to perform linear dynamic FEM analyses. This extension to the Guyan (1965) reduction adds eigenmodes to the modal basis to model the inertia of the internal degrees of freedom (DOFs), while static modes are used for the boundary DOFs. This approach proved efficient in performing parametric analyses on linear case studies but is limited when introducing nonlinearities.

Building reduced bases for nonlinear systems requires data-driven methods that use high-order reference solutions as training data, such as the proper orthogonal decomposition (POD) method (Karhunen, 1946; Kosambi, 1943; Loève, 1948). The POD was first applied to fluid dynamics models to identify coherent structures (Sirovich, 1987). It was later extended to turbulent flows modeling (Hall et al., 2000; Epureanu, 2003), dynamic systems control (Ravindran, 2000), damage detection (De Boe & Golinval, 2003), finite element model updating (Hemez & Doebling, 2001), and model order reduction in structural dynamics (Azeez & Vakakis, 1999). Recent works applied the POD to elastic–plastic reinforced concrete (RC) frame structures subjected to earthquakes (Ayoub et al., 2022).

Still, the time savings are limited when nonlinear terms of the reduced matrix system (e.g., restoring forces) need to be computed on the full basis as with nonlinear material laws. This problem can be solved by interpolating these terms using the response of a reduced set of elements included in a reduced integration domain (RID), where the physics is explicitly modeled. An interpolation operator, which is defined by high-dimensional training data, is used to approximate the nonlinear terms on the other parts of the mesh where the model properties are not updated. Such hyper-reduction methods are inherited from the "gappy" POD, which was developed to reconstruct facial images (Everson & Sirovich, 1995), to hyper-reduce nonlinear fluid dynamics systems (Bui-Thanh et al., 2003; Willcox, 2006), or to perform process simulations (Astrid, 2004).

An empirical "greedy" algorithm was later used to improve the selection of the RID components up to a relative tolerance set by the user (Chaturantabut & Sorensen, 2010). This contribution pushed forward the development of discrete empirical interpolation methods (DEIMs), commonly combined with the POD for building hyper-reduced order models (HROMs) to accelerate parametric FEM analyses. HROMs can model all kinds of physics that are introduced in the training dataset (e.g., damage, plasticity, or large deformations). As finite elements are linked to nodes defined by several DOFs, the RID usually includes more components than those selected by the "greedy" algorithm. Collocation techniques are commonly used to add all the computed components to the RID and improve the stability of the POD-DEIM (Rutzmoser, 2017). The force basis can also be built using unassembled force snapshots (i.e., computed element per element) to directly select the element that belongs to the RID instead of the DOFs when the greedy algorithm runs (Tiso & Rixen, 2013). Recent works showed that a better approximation is reached with smaller RIDs using the unassembled DEIM (UDEIM) since only elements where nonlinearities appear are selected (Rutzmoser, 2017).

Another possibility is to use a k-means clustering algorithm to classify the training data and define several reduced bases that are selected using a nearest-neighbor classifier (Ghavamian et al., 2017; Peherstorfer et al., 2014). Improved strategies could also be used to select

the collocation components (Drmac & Gugercin, 2016), alternatively to the method proposed by Chaturantabut and Sorensen (2010).

DEIM-based methods proved efficient in hyper reducing various physical parametric systems (Antil et al., 2014; Benner et al., 2015), which include strain-softening viscoplasticity (Ghavamian et al., 2017), large deformations with nonlinear hyper-elastic materials (Radermacher & Reese, 2016; Rutzmoser, 2017), nonlinear heat and moisture transfer (Hou et al., 2020), electro thermomechanical coupling (Roy & Nabi, 2021), magneto dynamics (Maierhofer & Rixen, 2022), or Stokes/Darcy coupling (Stoter et al., 2022). Hyper-reduction for accelerating dynamic analyses on damageable structures has never been investigated despite being promising for parametric analyses that use seismic databases.

To avoid iterating and save more CPU time, hyper-reduction could also be combined with a non-iterative α-operator splitting (α-OS) time integration, which was developed to perform dynamic FEM analyses during real-time hybrid tests on civil engineering structures (Nakashima et al., 1992). The α-OS method maintains the stability of the implicit Hilber–Hugues–Taylor (HHT; Hilber et al., 1977) method without iterating by splitting the restoring force vector into a linear part that depends on the elastic stiffness matrix and a nonlinear part computed once per time step using an explicit prediction of the displacement. An error is thus introduced, but Combescure et al. (1995) have shown that the α-OS method provides results quasi-identical to iterative implementations of the α-method under the infinitesimal strains assumption.

An extension of the POD-UDEIM for models involving softening damage laws with plastic dissipative mechanisms is proposed in this paper, with a focus on its robustness when performing parametric analyses on civil engineering structures subjected to earthquakes. The implicit Newmark and the α-OS methods also challenge the hyper-reduction procedure using seismic loadings that exceed the mechanical strength of the structures. A comparison between full and hyper-reduced solutions gives an overview of the possibilities HROMs offer for earthquake engineering analyses.

The non-iterative α-OS method is described in Section 2, while the POD-UDEIM procedure is detailed in Section 3. HROMs are then used in Section 4 to accelerate two parametric analyses on an RC frame building modeled using multi-fiber beam elements. Stiffness and mass centers are slightly off-center to induce torsion at floor level. The case study is voluntarily undersized to highlight the limitations of hyper-reduction and provides guidelines (e.g., truncation criterion or choice of the training data) that can be applied to most real-life applications, including highly damaged structures. The first analysis uses different ground motions as variables, while the second uses the orientation of the earthquake as a parameter.

2 | α-OS TIME INTEGRATION SCHEME

To avoid multiple reassessments of the tangent stiffness matrix and iterations at each time step, it is possible to use a non-iterative and unconditionally stable time integration scheme to perform nonlinear dynamic FEM analyses. The α-OS time integration scheme meets those requirements. This method was developed to solve the spatially discrete equation of motion during pseudo-dynamic hybrid tests on RC specimens (Pegon & Pinto, 2000).

The α-OS method is based on the classical HHT method (Hilber et al., 1977). Its originality lies in splitting the restoring force vector into a nonlinear part $\tilde{\boldsymbol{r}}^{\mathrm{NL}}(\tilde{\boldsymbol{u}})$, which is approximated using an explicit prediction of the displacements $\tilde{\boldsymbol{u}}$, and a linear part that depends on the elastic stiffness matrix (Nakashima et al., 1992):

$$\boldsymbol{r}(\boldsymbol{u}) \cong \boldsymbol{K}_{\mathrm{E}}\boldsymbol{u} + \tilde{\boldsymbol{r}}^{\mathrm{NL}}(\tilde{\boldsymbol{u}}) \tag{1}$$

where $\boldsymbol{K}_{\mathrm{E}}$ is the elastic stiffness matrix, and $\boldsymbol{u}$ is the displacement vector. At time step $n+1$, nonlinear material laws use the strains $\tilde{\boldsymbol{\varepsilon}}_{n+1}$, which are functions of $\tilde{\boldsymbol{u}}_{n+1}$, to update the stresses $\tilde{\boldsymbol{\sigma}}_n$, so $\tilde{\boldsymbol{\sigma}}_n(\tilde{\boldsymbol{\varepsilon}}_n) \rightarrow \tilde{\boldsymbol{\sigma}}_{n+1}(\tilde{\boldsymbol{\varepsilon}}_{n+1})$. The predicted restoring force vector $\tilde{\boldsymbol{r}}_{n+1}(\tilde{\boldsymbol{u}}_{n+1})$ is then built by integrating $\tilde{\boldsymbol{\sigma}}_{n+1}$ on each finite element. Its nonlinear part is defined as $\tilde{\boldsymbol{r}}^{\mathrm{NL}}_{n+1}(\tilde{\boldsymbol{u}}_{n+1}) = \tilde{\boldsymbol{r}}_{n+1}(\tilde{\boldsymbol{u}}_{n+1}) - \boldsymbol{K}_{\mathrm{E}}\tilde{\boldsymbol{u}}_{n+1}$. The system of linear equations to be solved to compute the acceleration vector $\ddot{\boldsymbol{u}}_{n+1}$ is given by introducing (1) into the equation of motion:

$$\hat{\boldsymbol{M}}\ddot{\boldsymbol{u}}_{n+1} = \hat{\boldsymbol{F}}_{n+1+\alpha} \tag{2}$$

where $\hat{\boldsymbol{M}}$ is the pseudo-mass matrix, and $\hat{\boldsymbol{F}}_{n+1+\alpha}$ is the pseudo-force vector (Pegon & Pinto, 2000). Note that this method depends on an α parameter usually set between $-1/3$ and 0, even if a value close to -0.05 is commonly used (Hilber et al., 1977).

The α-OS method is implicit in the linear phase and explicit in the nonlinear phase. No iteration is required since the predictive restoring force vector $\tilde{\boldsymbol{r}}_{n+1}(\tilde{\boldsymbol{u}}_{n+1})$ is assessed once per time step. In addition, as $\boldsymbol{K}_E$ is a constant, the matrix $\hat{\boldsymbol{M}}^{-1}$ is computed once before entering the time step loop, which decreases the CPU time. As demonstrated in practical cases, the residual error due to the approximation in (1) is almost negligible in the case of dynamic FEM analyses on RC structures subjected to infinitesimal strains (Combescure et al., 1995), which makes it suitable for earthquake engineering applications.

3 | USING A POD-UDEIM APPROACH

Using nonlinear material laws increases the CPU time necessary to compute the restoring force vector at each time step, even if a non-iterative time integration scheme is used. In addition, performing all the matrix operations on a full basis can also be time-consuming, especially if the structure has a high number of DOFs. To reduce the computational cost of the high-dimensional full-order model (FOM), a POD-UDEIM hyper-ROM approach is proposed.

The key idea of the POD is to first perform a small number of nonlinear FEM analyses on the FOM using variable loadings and/or several sets of mechanical properties. From these responses, N_S displacement vectors $\boldsymbol{u}(t) \in \mathbb{R}^{N_{\text{DOFs}}}$ (a.k.a, displacement snapshots) are then selected at different calculation times and stored in columns inside a sample matrix $\boldsymbol{S}_{\text{u}} \in \mathbb{R}^{N_{\text{DOFs}} \cdot N_{\text{S}}}$. Snapshots computed from different dynamic FEM analyses are mixed to capture the physics of the nonlinear parametric system for several loading paths. The components of $\boldsymbol{S}_{\text{u}}$ can be seen as discrete values of a function $s_{\text{u}}(\boldsymbol{x}, t)$ that can be approximated by a sum of N products of functions of space $\varphi_{i\,=\,1,\ldots,\,N}(\boldsymbol{x})$ and time $\kappa_{i\,=\,1,\ldots,\,N}(t)$ weighted by singular values $\lambda_{i\,=\,1,\ldots,\,N}$ (3):

$$s_{\text{u}}(\boldsymbol{x}, t) \approx \sum_{i\,=\,1}^{N} \varphi_i(\boldsymbol{x})\, \lambda_i \kappa_i(t) \tag{3}$$

where $N = \min(N_{DOFs}; N_S)$ is the number of products that can be built from the discrete training data. The discrete values of $\varphi_i(x)$ and $\kappa_i(t)$ stored in vectors $\boldsymbol{\varphi}_i$ and $\boldsymbol{\kappa}_i$ are computed performing a singular value decomposition (SVD) on $\boldsymbol{S}_{\text{u}}$ (Karhunen, 1946; Loève, 1948) (4):

$$\boldsymbol{S}_{\text{u}} \approx \boldsymbol{\Phi}\boldsymbol{\Lambda}\mathbf{K}^{\text{T}} = \begin{bmatrix} \boldsymbol{\varphi}_1 \ldots \boldsymbol{\varphi}_N \end{bmatrix} \begin{bmatrix} \lambda_1 & 0 & 0 \\ 0 & \ddots & 0 \\ 0 & 0 & \lambda_N \end{bmatrix} \begin{bmatrix} \boldsymbol{\kappa}_i^{\text{T}} \\ \vdots \\ \boldsymbol{\kappa}_N^{\text{T}} \end{bmatrix} \tag{4}$$

where $\boldsymbol{\Phi} \in \mathbb{R}^{N_{DOFs} \times N}$ is a displacement modal basis made of N POD modes $\boldsymbol{\varphi}_i$. The similarity of a POD mode with the training dataset is quantified by its singular value λ_i, whose value decreases as the order i increases. As low singular values refer to POD modes whose contribution to the response is almost negligible, the basis $\boldsymbol{\Phi}$ can be truncated as described in (5):

$$1 - \frac{\sum_{i\,=\,1}^{n} \lambda_i}{\sum_{j\,=\,1}^{N} \lambda_j} \leq \varepsilon \tag{5}$$

where $n \ll N$ is the number of POD modes in the truncated modal basis, λ_i the singular value of the ith POD mode, and ε is a tolerance usually set to 10^{-2} (Ayoub et al., 2022). As the singular values are summed from the lowest to the highest order, the truncation criterion in (5) converges toward a constant value since $\lim_{i \to N} \lambda_i = 0$. The displacement vector $\boldsymbol{u} \in \mathbb{R}^{N_{DOFs}}$ can thus be expressed in a new basis $\boldsymbol{\Phi} \in \mathbb{R}^{N_{\text{DOFs}} \times n}$ as described in (6):

$$\boldsymbol{u} \approx \boldsymbol{\Phi}\boldsymbol{q} \qquad with \qquad \boldsymbol{\Phi} = \begin{bmatrix} \boldsymbol{\varphi}_1 \cdots \boldsymbol{\varphi}_n \end{bmatrix} \tag{6}$$

where $\boldsymbol{q} \in \mathbb{R}^n$ is the reduced displacement vector. The number of DOFs, as well as the computational cost of the matrix operations, are thus significantly reduced. Note that displacement snapshots defined using several loadings (e.g., earthquake or wind) and/or mechanical properties (e.g., dimensions or material law parameters) could be combined to expand the applicability of the ROM, even if this decreases the efficiency of the method since more POD modes are required to correctly model the variability of the nonlinear parametric system.

A UDEIM operator is also added to the solving process to avoid updating the material properties on the entire mesh (Tiso & Rixen, 2013). Similarly to (3) and (4), a force basis is built using force snapshots defined using the nonlinear part of the unassembled restoring force vector $\boldsymbol{r}^{\text{NL,u}} \in \mathbb{R}^{N_e \cdot N_c}$ (i.e., computed element per element). Let N_e be the number of finite elements and N_c the number of force components per element. When the α-OS method is used, the explicit prediction of $\boldsymbol{r}^{\text{NL,u}}$ defined in (1) is taken as a force snapshot, resulting in:

$$\tilde{\boldsymbol{r}}^{\text{NL,u}} = \tilde{\boldsymbol{r}}^{\text{u}}(\tilde{\boldsymbol{u}}) - \boldsymbol{K}_{\text{E}}^{\text{u}} \boldsymbol{B} \tilde{\boldsymbol{u}} \tag{7}$$

where $\boldsymbol{K}_{\text{E}}^{\text{u}} \in \mathbb{R}^{N_e \cdot N_c \times N_e \cdot N_c}$ is the unassembled elastic stiffness matrix, $\boldsymbol{B} = [\boldsymbol{L}_1^T \cdots \boldsymbol{L}_{N_e}^T]^T \in \mathbb{R}^{N_e \cdot N_c \times N_{DOFs}}$ is a Boolean assembly matrix, and $\boldsymbol{L}_{i\,=\,1,\ldots,\,N_e} \in \mathbb{R}^{N_c \times N_{DOFs}}$ is a collocation matrix used to select the displacements of the nodes connected to the i^{th} finite element (8):

$$\tilde{\boldsymbol{r}}^{\text{u}} = \begin{pmatrix} \tilde{\boldsymbol{r}}_1^{\text{u}} \\ \vdots \\ \tilde{\boldsymbol{r}}_{N_e}^{\text{u}} \end{pmatrix} \quad \& \quad \boldsymbol{K}_{\text{E}}^{\text{u}} = \begin{pmatrix} \boldsymbol{K}_{\text{E},1}^{\text{u}} & \ldots & 0 \\ \vdots & \ddots & \vdots \\ 0 & \ldots & \boldsymbol{K}_{\text{E},N_e}^{\text{u}} \end{pmatrix} \tag{8}$$

The m first UDEIM modes are then selected according to (5) to build a second truncated modal basis $\boldsymbol{\Psi} \in \mathbb{R}^{N_e \cdot N_c \times m}$. So $\tilde{\boldsymbol{r}}^{\text{NL,u}} \cong \boldsymbol{\Psi}\boldsymbol{c}$ where $\boldsymbol{c} \in \mathbb{R}^m$ is the vector containing the scalar weights associated with the truncated modal basis $\boldsymbol{\Psi} = [\psi_1 \cdots \psi_m]$. It should be noted that since the tolerance ε used for the truncation of $\boldsymbol{\Psi}$ defines the number of collocation components, its value may depend on the physics of the case study. A sensitivity analysis could thus be necessary to assess ε. When m is known, the greedy Algorithm 1 is then used to find for each UDEIM mode $\boldsymbol{\psi}_i \in \mathbb{R}^{N_e \cdot N_c}$ the best collocation component (i.e., indexed

ALGORITHM 1 DEIM algorithm

Input: A set of DEIM modes $\boldsymbol{\Psi} = [\,\boldsymbol{\psi}_1 \;\cdots\; \boldsymbol{\psi}_m\,]$

Output: Index of the interpolation DOFs $\boldsymbol{ID} = [\,ID_1 \;\cdots\; ID_m\,]$ and partition matrix $\boldsymbol{P} = [\,\boldsymbol{p}_1 \;\ldots\; \boldsymbol{p}_m\,]$

Set ID_1 = index of the maximum component of $|\boldsymbol{\psi}_1|$

Set $\boldsymbol{I}_d = [\,\boldsymbol{e}_1 \;\ldots\; \boldsymbol{e}_{N_e \cdot N_c}\,]$ the identity matrix of size $N_e \cdot N_c \times N_e \cdot N_c$

Initiate matrices: $\boldsymbol{V} = [\boldsymbol{\psi}_1]$, $\boldsymbol{P} = [\boldsymbol{e}_{ID_1}]$, $\boldsymbol{ID} = [ID_1]$

For $i = 2,\ldots, m$ do

Solve $\boldsymbol{P}^{\mathrm{T}}\boldsymbol{V}\boldsymbol{c}_i = \boldsymbol{P}^{\mathrm{T}}\boldsymbol{\psi}_i$

Compute residual $\boldsymbol{res} = |\boldsymbol{\psi}_i - \boldsymbol{V}\boldsymbol{c}_i|$

Set ID_i = index of the maximum component of $\boldsymbol{res}$

Augment $\boldsymbol{V} \leftarrow [\,\boldsymbol{V}\;\boldsymbol{\psi}_i\,]$, $\boldsymbol{P} \leftarrow [\,\boldsymbol{P}\;\boldsymbol{e}_{ID_i}\,]$, $\boldsymbol{ID} \leftarrow [\,\boldsymbol{ID}\;ID_i\,]$

End

ID_i) related to the maximum value of the residual $\boldsymbol{res} = |\boldsymbol{\psi}_i - \boldsymbol{V}\boldsymbol{c}_i|$.

Let $\boldsymbol{V} \in \mathbb{R}^{N_e \cdot N_c \times (i-1)}$ be a basis made of the $i-1$ first UDEIM modes and $\boldsymbol{c}_i$ the scalar weights computed by solving $\boldsymbol{P}^T\boldsymbol{V}\boldsymbol{c}_i = \boldsymbol{P}^T\boldsymbol{\psi}_i$, where $\boldsymbol{P} \in \mathbb{R}^{N_e \cdot N_c \times (i-1)}$ is the Boolean partition matrix used to select the collocation components. When the component related to the ith mode is known, the column $\boldsymbol{e}_{ID_i}$ of the $\boldsymbol{I}_d \in \mathbb{R}^{N_e \cdot N_c \times N_e \cdot N_c}$ identity matrix is added to the partition matrix, so $\boldsymbol{P} \leftarrow [\,\boldsymbol{P}\;\boldsymbol{e}_{ID_i}\,]$ and $\boldsymbol{V} \leftarrow [\,\boldsymbol{V}\;\boldsymbol{\psi}_i\,]$. These steps are repeated until all the m collocation components are known.

When the UDEIM is used with implicit time integration methods, the tangent operator must also be interpolated during the solving process. As the symmetry of the approximated tangent operator is not kept, difficulties for converging (i.e., numerical instabilities) appear over time as nonlinear mechanisms (e.g., large deformations, damage, friction, or hardening) occur. To preserve as much as possible the symmetry of the matrix system, the unassembled tangent operator $\boldsymbol{K}_{\mathrm{T}}^{\mathrm{u}}$ is redefined as a sum of $\boldsymbol{K}_{\mathrm{E}}^{\mathrm{u}}$ (7), which is constant and symmetric, with an asymmetric correction $\Delta\boldsymbol{K}_{\mathrm{T}}^{\mathrm{u}}$ that is approximated during the online phases (i.e., nonlinear FEM analyses where the hyper-reduced matrix system is solved on the reduced basis $\boldsymbol{\Phi}$). As the tangent operator is only interpolated on the elements where nonlinear mechanisms appear, the robustness of the UDEIM is improved, even if the convergence is still not guaranteed. To avoid numerical instabilities, it is possible to add the unused components of the RID to the partition matrix $\boldsymbol{P} \in \mathbb{R}^{N_e \cdot N_c \times m}$. The number of collocation components k is thus higher than the number m of UDEIM modes (i.e., $k > m$). Considering a new partition matrix $\boldsymbol{P} \in \mathbb{R}^{N_e \cdot N_c \times k}$ leads to an overdetermined matrix system $\boldsymbol{P}^{\mathrm{T}}\boldsymbol{\psi}\boldsymbol{c} \approx \boldsymbol{P}^{\mathrm{T}}\tilde{\boldsymbol{r}}^{\mathrm{NL,u}}$. The scalar weights $\boldsymbol{c} \in \mathbb{R}^m$ are thus computed in the least square sense using a Monroe–Penrose pseudo-inverse $(\cdot)^+$ to minimize residual in the L^2-norm, leading to $\boldsymbol{c} \approx (\boldsymbol{P}^{\mathrm{T}}\boldsymbol{\psi})^+\boldsymbol{P}^{\mathrm{T}}\tilde{\boldsymbol{r}}^{\mathrm{NL,u}}$. It should be noted that when Algorithm 1 runs, the selection of the collocation components could be improved by directly adding the additional components to $\boldsymbol{P}$ (Rutzmoser, 2017). Unfortunately, the computational cost of Algorithm 1 increases drastically since the size of the matrix system solved at each iteration is N_c times higher. In addition, the accuracy of the interpolation operator does not change significantly. The additional components are thus added to $\boldsymbol{P}$ a posteriori (i.e., when the RID is already defined).

When the k collocation components are set, the online phases proceed. The material laws are updated on the elements belonging to the RID (i.e., where the nonlinear part of the unassembled restoring force vector needs to be computed). The k collocation components stored in $\tilde{\boldsymbol{r}}_{\mathrm{RID}}^{\mathrm{NL,u}} = \boldsymbol{P}^{\mathrm{T}}\tilde{\boldsymbol{r}}^{\mathrm{NL,u}} \in \mathbb{R}^k$ are then used as samples to build the vector $\tilde{\boldsymbol{r}} \in \mathbb{R}^{N_{DOFs}}$ on the entire domain as described in (9):

$$\begin{aligned} \tilde{\boldsymbol{r}}(\Phi\tilde{\boldsymbol{q}}) &= \boldsymbol{B}^{\mathrm{T}}\left(\boldsymbol{K}_{\mathrm{E}}^{\mathrm{u}}\boldsymbol{B}\Phi\tilde{\boldsymbol{q}} + \boldsymbol{A}\tilde{\boldsymbol{r}}_{\mathrm{RID}}^{\mathrm{NL,u}}(\Phi\tilde{\boldsymbol{q}})\right) \\ \boldsymbol{A} &= \boldsymbol{\Psi}\left(\boldsymbol{P}^{\mathrm{T}}\boldsymbol{\Psi}\right)^+ \end{aligned} \tag{9}$$

where $\boldsymbol{K}_{\mathrm{E}}^{\mathrm{u}} \in \mathbb{R}^{N_e \cdot N_c \times N_e \cdot N_c}$ is the unassembled elastic stiffness matrix, $\boldsymbol{\Phi} \in \mathbb{R}^{N_{DOFs} \times n}$ is the basis of POD modes, $\tilde{\boldsymbol{q}} \in \mathbb{R}^n$ is the prediction of the displacement vector in basis $\boldsymbol{\Phi}$, $\boldsymbol{\Psi} \in \mathbb{R}^{N_e \cdot N_c \times m}$ is the basis of UDEIM modes, $\boldsymbol{P} \in \mathbb{R}^{N_e \cdot N_c \times k}$ is the partition matrix, and $\boldsymbol{A} \in \mathbb{R}^{N_e \cdot N_c \times k}$ is the UDEIM interpolation operator. As a result, according to (7), (9) becomes:

$$\tilde{\boldsymbol{r}}(\boldsymbol{\Phi}\tilde{\boldsymbol{q}}) = \boldsymbol{B}^{\mathrm{T}}\left(\boldsymbol{I}_{\mathrm{d}} - \boldsymbol{A}\boldsymbol{P}^{\mathrm{T}}\right)\boldsymbol{K}_{\mathrm{E}}^{\mathrm{u}}\boldsymbol{B}\boldsymbol{\Phi}\tilde{\boldsymbol{q}} + \boldsymbol{B}^{\mathrm{T}}\boldsymbol{A}\tilde{\boldsymbol{r}}_{\mathrm{RID}}^{\mathrm{u}}(\boldsymbol{\Phi}\tilde{\boldsymbol{q}}) \tag{10}$$

where $\boldsymbol{I}_{\mathrm{d}} \in \mathbb{R}^{N_e \cdot N_c \times N_e \cdot N_c}$ is an identity matrix, and $\tilde{\boldsymbol{r}}_{\mathrm{RID}}^{\mathrm{u}}(\boldsymbol{\Phi}\tilde{\boldsymbol{q}}) \in \mathbb{R}^k$ is the prediction of the unassembled restoring force vector assessed on the k collocation components belonging to the RID. During the online phase, the acceleration vector $\ddot{\boldsymbol{q}} \in \mathbb{R}^n$ in the reduced basis Φ is computed at time step $n+1$ as described in (11):

$$\ddot{\boldsymbol{q}}_{n+1} = \left(\boldsymbol{\Phi}^{\mathrm{T}}\widehat{\boldsymbol{M}}\boldsymbol{\Phi}\right)^{-1}\boldsymbol{\Phi}^{\mathrm{T}}\widehat{\boldsymbol{F}}_{n+1+\alpha}(\boldsymbol{\Phi}\tilde{\boldsymbol{q}}_{n+1}) \tag{11}$$

Even if iterations are avoided with the α-OS method, they are still required when the HROM is used to perform static or implicit dynamic FEM analyses. In these cases, the reduced tangent stiffness matrix $\tilde{\boldsymbol{K}}_T \in \mathbb{R}^{n \times n}$

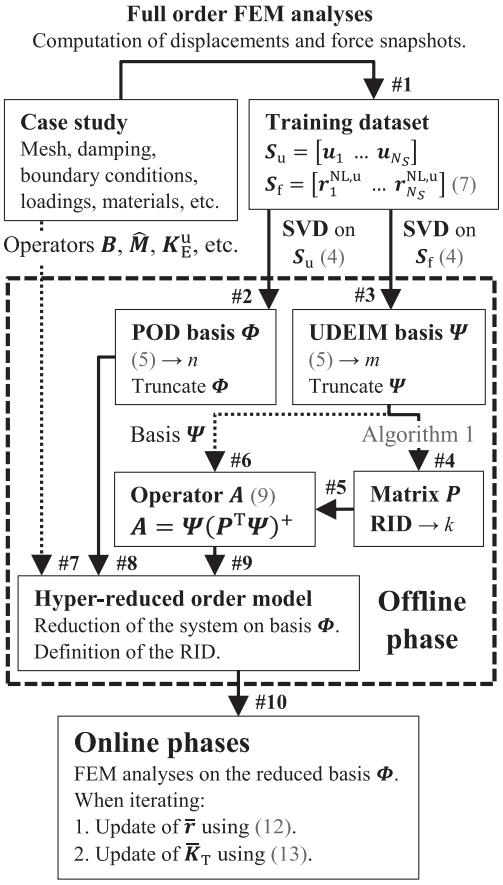

FIGURE 1 Proper orthogonal decomposition–discrete empirical interpolation method (POD-UDEIM) hyper-reduction procedure. RID, reduced integration domain.

and the reduced restoring force vector $\bar{\boldsymbol{r}}(\boldsymbol{\Phi q}) \in \mathbb{R}^n$ need to be updated when iterating. As a result, (10) becomes:

$$\bar{\boldsymbol{r}}(\boldsymbol{\Phi q}) = \boldsymbol{\Phi}^T\boldsymbol{B}^T\left(\boldsymbol{I}_d - \boldsymbol{A}\boldsymbol{P}^T\right)\boldsymbol{K}_E^u\boldsymbol{B}\boldsymbol{\Phi q} + \boldsymbol{\Phi}^T\boldsymbol{B}^T\boldsymbol{A}\boldsymbol{r}_{RID}^u(\boldsymbol{\Phi q}) \tag{12}$$

where $\boldsymbol{r}_{RID}^u(\boldsymbol{\Phi q}) \in \mathbb{R}^k$ is the unassembled restoring force vector assessed on the k collocation components belonging to the RID. The reduced tangent stiffness matrix $\bar{\boldsymbol{K}}_T$ can thus be approximated by derivation of (12) with respect to $\boldsymbol{q}$ (13):

$$\begin{aligned}\bar{\boldsymbol{K}}_T &= \frac{\partial\bar{\boldsymbol{r}}(\boldsymbol{\Phi q})}{\partial\boldsymbol{q}}\\ \bar{\boldsymbol{K}}_T &\approx \boldsymbol{\Phi}^T\boldsymbol{B}^T\left(\left(\boldsymbol{I}_d - \boldsymbol{A}\boldsymbol{P}^T\right)\boldsymbol{K}_E^u + \boldsymbol{A}K_{T,RID}^u\right)\boldsymbol{B}\boldsymbol{\Phi}\end{aligned} \tag{13}$$

where $\boldsymbol{K}_{T,RID}^u = \frac{\partial\boldsymbol{r}_{RID}^u(\boldsymbol{\Phi q})}{\partial\boldsymbol{B}\boldsymbol{\Phi q}} = \boldsymbol{P}^T\frac{\partial\boldsymbol{r}^u(\boldsymbol{\Phi q})}{\partial\boldsymbol{B}\boldsymbol{\Phi q}} \in \mathbb{R}^{k\times N_e\cdot N_c}$ is the unassembled tangent stiffness matrix related to the k collocation components included in the RID, computed when iterating and used as a sample to approximate $\bar{\boldsymbol{K}}_T$. The hyper-reduction procedure is summarized in the block scheme in Figure 1.

It should be noted that the accuracy of the POD-UDEIM hyper-reduction method highly depends upon k. Even if refined meshes could amplify local nonlinearities and lead to higher k values, this phenomenon is limited since the system is projected on a POD displacement basis that regularizes the physics and avoids an excessive mesh dependency. The number k of components in the RID thus increases proportionally to the number of nonlinear elements in the training dataset (e.g., where damage appears). In addition, k also depends on the variability of the force snapshots that define the limits of the parametric system since a bigger RID is required to correctly approximate the nonlinear response when several settings may vary simultaneously. As the singular values well capture this variability, the force basis can be efficiently truncated using a tolerance ε usually set between 10^{-4} and 10^{-2} (5). Even if 10^{-2} is usually recommended for ε, lower values can be required for nonlinear systems that use complex materials laws defined by loading path-dependent internal variables, which can be hard to approximate on a reduced basis, as is the case for concrete on the present work (see Section 4.1).

A sensitivity analysis will be performed on a practical case in Section 4.5 to find the tolerance ε to use for the truncation of the force basis $\boldsymbol{\Psi}$ to ensure a good accuracy of the results with significant CPU time-savings. The efficiency of hyper-reduction in accelerating earthquake engineering parametric analyses about the loading properties will then be discussed.

4 | APPLICATIONS

4.1 | Numerical modeling of RC structures

The global kinematics of the following case study was modeled with Timoshenko multi-fiber beam elements defined by quadratic and cubic shape functions for the bending rotations and the transverse displacements, respectively (Davenne et al., 2003). An example of multi-fiber mesh for a simply supported RC beam is presented in Figure 2.

The integration points were linked to sections made of nonlinear fibers. The deformations of those fibers were assessed using the beam kinematics under the assumption that the sections remain flat. The material properties were locally updated on concrete fibers located at the integration points of meshes that defined the cross-sections of the beams (see Figure 2b), but also on additional steel fibers that modeled the longitudinal reinforcements (see Figure 2a). The surface meshes were located at the Gauss points of the beam elements. The restoring force vector was computed by double integrating the stresses: on the sections to evaluate the generalized stresses at the Gauss

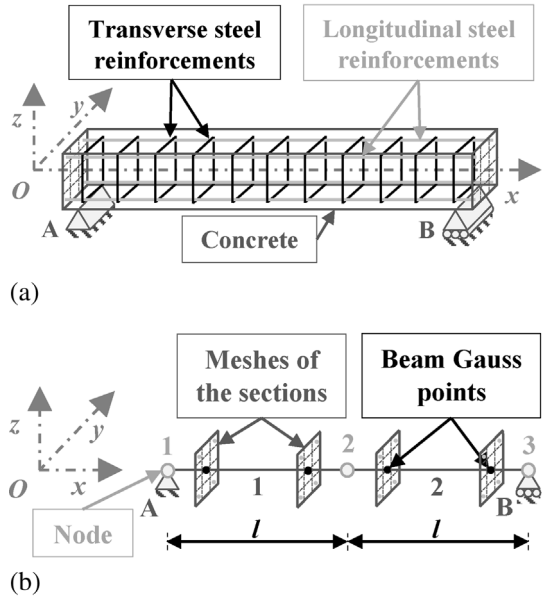

FIGURE 2 Reinforced concrete beam with simple supports (a) and multi-fiber mesh with two Timoshenko beam elements (b).

points and on the beam elements to compute the restoring forces at the nodes. Knowing that the length/height ratio of the structural components (e.g., beams or columns) is usually higher than 10 for civil engineering frame structures, the damage was assumed to be mainly due to bending (Davenne et al., 2003). As a result, only one-dimensional (1D) nonlinear material laws were used, while shear and torsion remained elastic. The transverse steel reinforcements were also assumed to prevent shearing failure mechanisms since they were not explicitly included in the multi-fiber mesh, even if experiments and post-seismic inspections proved that such phenomena could also appear on short beams and columns as well as on column/beam connections subjected to cyclic loadings (Alcocer et al., 2020). A better modeling of concrete shearing could have been achieved using a 2D plane strain material law, even if modeling accurately shearing failure mechanisms still requires 3D finite elements linked to 1D steel reinforcements (Hervé-Secourgeon et al., 2021), which was not addressed in this work. Multilayer plates or shells could also have been used to model membrane components (e.g., walls or slabs), as well as nonlinear macro elements to model the RC column/beam connections using homogenized properties that depend on the steel reinforcements (Pantò et al., 2021).

Many material laws can be used to model the behavior of RC frame structures. If elastic plastic hinges are well suited for homogenized cross-sections (Hafezolghorani et al., 2022), the multi-fiber beam element support allows for the use of quasi-brittle damage laws that are locally applied to the concrete fibers (see Figure 6c).

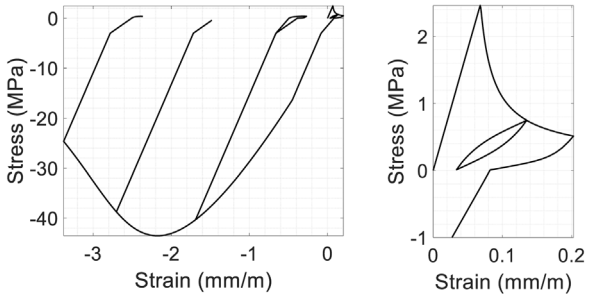

FIGURE 3 One-dimensional damage law for concrete with opening/closing of cracks (a) and frictional sliding (b).

Under dynamic or cyclic loadings, damage leads to softening and hysteretic energy dissipations due to frictional sliding but also to a progressive recovery of the secant modulus when the cracks are closing. A quasi-brittle damage law that model accurately all these phenomena (Richard & Ragueneau, 2013) was used for concrete (see Figure 3).

The parameters of the concrete material law were set according to experiments (Terrien, 1980). Here, an elastic modulus of 36 GPa and a Poisson's ratio of 0.2 were considered. The damage-yielding surface was defined by an initial energy threshold of 83 J/m^3 and a brittleness coefficient of 2.9×10^{-2} m^3/J. The frictional sliding evolution depended on a kinematic hardening surface modulus of 7.0×10^9 Pa and a kinematic hardening pseudo-potential modulus of 7.0×10^{-6} Pa^{-1}. The cracks were closed when the stresses were lower than a mean closure value of −3.0 MPa, while the hardening appeared in compression when a strength of −15 MPa was reached. The evolution of the hardening was defined by a plastic surface modulus of 0.25, a plastic pseudo-potential modulus of 0.91 for modeling the dilatancy, a plastic hardening modulus of 55 GPa, and a plastic hardening coefficient of 600 that drove the softening. The CPU time heavily increased when concrete dissipative mechanisms occurred. Modeling them was costly since internal variables had to be updated using a return-mapping algorithm with strain sub increments lower than 10^{-5} m/m to converge (Richard & Ragueneau, 2013). A lower initial energy threshold (i.e., tensile strength) would have led to higher CPU times since damage, softening, and frictional sliding loops would have appeared earlier.

Cyclic movements also generated kinematic hardening of the steel reinforcements. These mechanisms were modeled on the steel fibers using a bilinear elastic–plastic law defined by an elastic modulus of 210 GPa, a yielding stress of 500 MPa, and a kinematic hardening modulus of 1000 MPa.

4.2 | Case study

Simulations were performed on a two-story RC building subjected to earthquakes to challenge the efficiency of the POD-UDEIM hyper-ROM method in accurately approximating nonlinear structural dynamic responses at a lower computational cost. All the simulations were carried out using custom procedures implemented in MATLAB software. The seismic hazard was modeled by a set of 12 natural ground motions recorded at Friuli on May 6, 1976, Montenegro on April 15, 1979, and May 25, 1979, Adana on July 27, 1998, Alkion on February 24, 1981, Izmit on August 17, 1999, Kalamata on September 13, 1986, and Umbria Marche on September 26, 1997. All these earthquakes were modified by Diana et al. (2018) using a non-stationary spectral matching method to fit the design spectrum of the "Rhonetal" microzoning area around the city of Visp in Switzerland. All the ground motions were sampled at 100 Hz. Even if these signals are of the same order of magnitude (i.e., with a peak ground acceleration [PGA] between 2.3 and 2.8 m/s^2), their frequency, strong motion duration, and number of aftershocks differed (see Figure 4). Three were first used to compute the snapshots, the POD modal basis $\boldsymbol{\Phi}$, and the UDEIM interpolation operator $\boldsymbol{A}$. The responses related to the nine others were approximated using hyper-reduction. The pseudo-acceleration floor response spectra at ground level with a damping ratio of 5% are compared to the design spectrum in Figure 5.

The case study was a two-story RC building defined by 1555 nodes linked by 1712 multi-fiber beam elements (see Figure 6a). All the columns were embedded to the floor level, and 9222 free DOFs modeled the structure. Both stories were 3-m high, each with spans of 3 m. The beam elements were 25-cm long, and a center-to-center distance of 1 m was applied to the transverse and the longitudinal beams for modeling the floors. A stairwell occupying an area of 2 × 2 m^2 was located at the northwest corner of the building and was modeled by three columns, which increased the stiffness locally. A mass per unit area of 500 kg/m^2 was applied to both floors via the longitudinal beams, whereas the mass of the stairwell was neglected. To model the mass of the structural components, densities of 2350 and 7850 kg/m^3 were used for the concrete and the steel, respectively.

As HROMs are most of the time used to model smooth physics with moderate nonlinearities, small sections were used for the structural components to be sure that earthquakes induce significant nonlinear dissipative mechanisms (e.g., damage with softening or frictional sliding) that challenge the applicability of hyper-reduction.

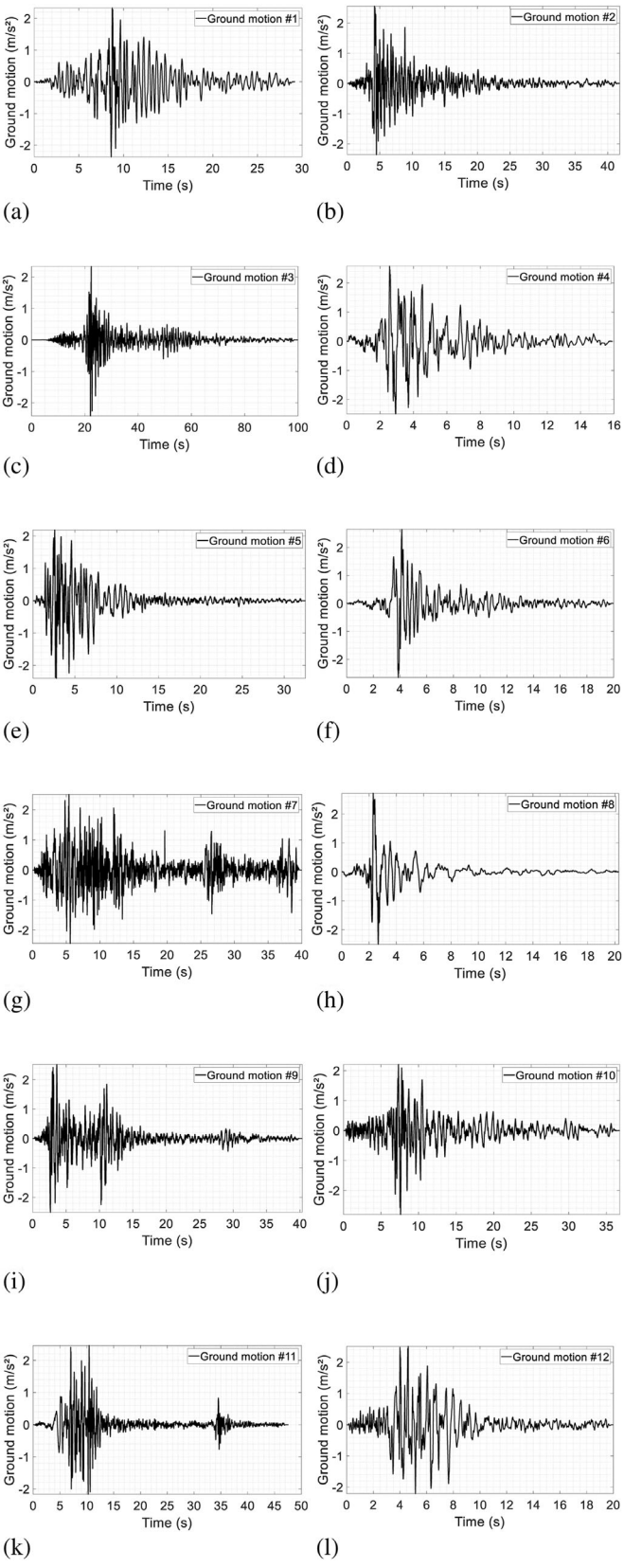

FIGURE 4 Set of 12 natural ground motions modified to fit the design spectrum of the "Rhonetal" area around the city of Visp in Switzerland.

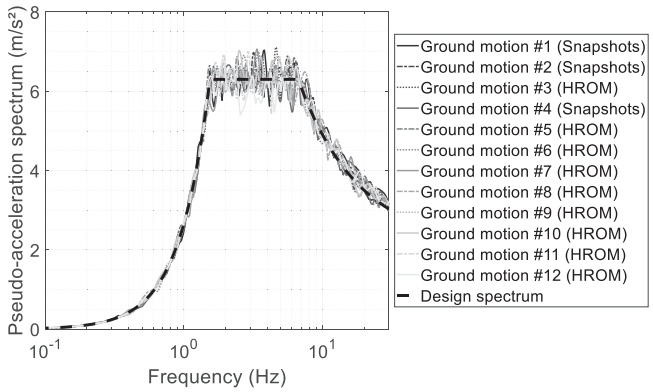

FIGURE 5 Pseudo-acceleration spectra related to the 12 ground motions with $\xi = 5\%$. HROM, hyper-reduced order model.

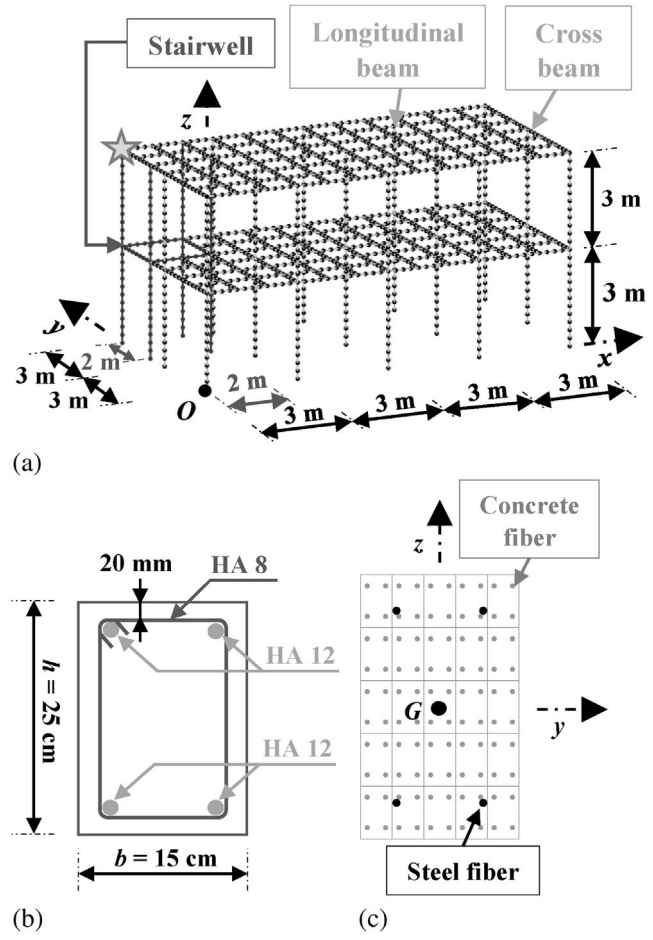

FIGURE 6 Mesh of the building (a), cross-section of the beams (b), and mesh of the cross-section of the beams (c).

The columns had a 15 × 15 cm square cross-section, and the beams had a 15 × 25 cm rectangular one. The diameter of each longitudinal steel reinforcement was set at 12 mm, and the concrete cover was 20 mm (see Figure 6b). All the cross-sections were divided into 5 × 5 surface elements, each using four integration points with linear shape functions for integrating the local stresses (see Figure 6c). The nonlinear material laws were thus locally applied to 356,100 fibers distributed on 3424 sections (i.e., two per beam element), which significantly increased the complexity of the multi-fiber beam model. All in all, 342,400 concrete fibers were located at the integration points of the surface elements (see the gray dots), while 13,700 steel fibers (see the black dots) were located at 34 mm from the corners of the cross-sections.

TABLE 1 Main eigenfrequencies and percentages of effective modal mass of the model.

Eigenfrequency (Hz)	% of the effective modal mass		
	x-axis	*y*-axis	*z*-axis
1.41	6.84	76.7	~0
1.47	84.6	7.92	~0
1.90	1.12	7.81	~0
3.82	0.40	5.31	~0
4.01	5.80	0.49	~0
5.23	0.09	0.59	~0
12.3	~0	~0	~0

The main eigenmodes and percentages of effective modal mass are summarized in Table 1. The structure weighed 108 tons and was mainly affected by the six first eigenmodes, with a cumulative modal mass reaching 106 tons (i.e., 98.8% of the total mass). A Rayleigh viscous damping ratio was applied with respect to this frequency range to arbitrarily model additional dissipative mechanisms (e.g., thermal breaks or friction between steel reinforcements and concrete) that appear on actual structures and are not included in the physics of the multi-fiber mesh.

As recommended for damageable RC buildings (Chambreuil, 2022), the damping ratio was set at $\xi = 2\%$ at $f_1 = 1.41$ Hz (i.e., eigenfrequency #1) and $f_6 = 5.23$ Hz (i.e., eigenfrequency #6) so that its value reached a minimum around the main eigenmodes.

The damping matrix was thus equal to $\boldsymbol{C} = \alpha_M \boldsymbol{M} + \beta_M \boldsymbol{K}_E$ with $\alpha_M = 4 \cdot \pi \cdot \xi \cdot f_1 \cdot f_6 \cdot (f_1 - f_6)/(f_1^2 - f_6^2)$ and $\beta_M = \xi/\pi \cdot (f_1 - f_6)/(f_1^2 - f_6^2)$ (Rayleigh, 1896), so $\alpha_M = 0.28$ rad/s and $\beta_M = 9.58 \times 10^{-4}$ s/rad. To induce high damage levels, the ground motions were all weighted by 1.0 in the *x*-direction, −0.7 in the *y*-direction, and 0.3 in the *z*-direction. The dead and live loads were statically applied before entering the time step loop.

4.3 | Choice of the training data

Training data extracted from simulations that lead to high damage levels are required to ensure that HROMs

can correctly approximate the restoring forces when dissipative mechanisms appear on a large set of elements. References solutions computed using ground motions either having the highest PGA, peak ground displacement (PGD), and peak ground velocity (PGV) or activating the main eigenfrequencies of the model could be used for this purpose (Ayoub et al., 2022). Such indicators are commonly correlated with the structural damage level since the PGA, the PGV, and the PGD are defined as the maximum acceleration, velocity, and displacement at ground level, respectively (Lai et al., 2022). The training dataset must also include snapshots computed with earthquakes of moderate intensity that best represent the expected average structural response of the parametric system. Such mixed data improve the approximation of the restoring forces vector using the force basis $\mathbf{\Psi}$, regardless of the evolution of the loading path-dependent internal variables within the RID. Thus, the range of physical mechanisms that can be simulated becomes larger.

Two criteria were applied to select earthquakes that lead to high damage levels. The average band-limited power P_{BL} contained around the main eigenfrequencies of the model was used first. It quantifies the ability of an earthquake to activate the main eigenmodes of the model (i.e., between $f_{\min}$ and $f_{\max}$ here) and takes into account the amplitude of the PGA since the acceleration of the ground $\ddot{u}_g(t)$ is used to compute the energy spectral density $\bar{S}_{xx}(f)$ as described in (14):

$$P_{BL} = 2\int_{f_{min}}^{f_{max}} \bar{S}_{xx}(f)\, df \text{ with } \bar{S}_{xx}(f) = \frac{|\hat{x}(f)|^2}{f_s} \quad (14)$$

where $\hat{x}(f)$ is the discrete fast Fourier transform of the ground motion $\ddot{u}_g(t)$ (computed using 2^{15} samples with zero-padding), and $f_s = 100$ Hz is the sampling frequency. An integration interval between $f_1 = 1.41$ Hz (eigenfrequency #1) and $f_5 = 4.01$ Hz (eigenfrequency #5) was used. The eigenfrequency #6 was not included since its percentage of effective modal mass was almost negligible (i.e., less than 1%, see Table 1). The main bending and torsional eigenmodes are expected to be strongly activated with earthquakes that maximize P_{BL}. As the amplitude of the cycles is higher with such ground motions, the strains increase, as well as the damage level.

The PGV, computed by integrating the ground motion over time, is also a good indicator since high values refer to strong-intensity earthquakes that are more likely to cause significant damage (Alcocer et al., 2020). However, the PGD was not used here to select earthquakes, as it is more suited for tall structures (Lai et al., 2022). All these criteria are summarized in Table 2.

TABLE 2 Peak ground acceleration (PGA), peak ground velocity (PGV), peak ground displacement (PGD), and average band-limited power of each ground motion.

Ground motion	PGA (m/s^2)	PGV (m/s)	PGD (m)	P_{BL} ($m^2 \cdot s^{-3}$)
# 1	2.37	0.163	0.053	4.28
# 2	2.56	0.256	0.057	4.00
# 3	2.41	0.171	0.048	3.30
# 4	2.58	0.208	0.050	2.54
# 5	2.39	0.179	0.041	3.42
# 6	2.64	0.202	0.134	2.24
# 7	2.51	0.212	0.179	3.13
# 8	2.70	0.249	0.310	1.52
# 9	2.51	0.189	0.086	3.93
# 10	2.80	0.196	0.182	3.41
# 11	2.46	0.175	0.095	2.93
# 12	2.51	0.184	0.045	2.75

It should be noted that high PGAs do not necessarily lead to high PGVs in the case of ground motions defined by high natural frequencies. Among the set of available earthquakes, #1 and #2 exhibit the highest average band-limited power, with values equal to 4.28 and 4.00 $m^2 \cdot s^{-3}$, respectively. They are thus more likely to activate the main eigenmodes. In addition, the highest PGV (i.e., 0.256 m/s) was recorded on ground motion #2, making it even more relevant for the computation of snapshots.

To complete the set of training data, an earthquake of moderate intensity has to take intermediate damage levels into account. Ground motions #4, #6, and #12, which are defined by moderate average-band limited powers between 2 and 3 $m^2 \cdot s^{-3}$, could be used for this purpose since they are most likely to be representative of the average response of the parametric system. As it is the shortest, #4 was used since less CPU time is required to compute the nonlinear dynamic response of the FOM. Other indicators than P_{BL} could be used to determine the intensity of ground motions (e.g., Housner intensity, significant duration, or cumulative absolute velocity; Lai et al., 2022). A detailed sensitivity analysis, which is not carried out in this paper, would be helpful to find the best indicators for selecting ground motions that are representative of entire seismic databases that need to be simulated on structural models. Efficient HROMs could thus be built using the selected ground motions for accelerating parametric analyses (e.g., fragility curves).

4.4 | Accuracy of the α-OS method

Following the conclusions of Section 4.3, the HROM was built using a set of 2899 snapshots based on the

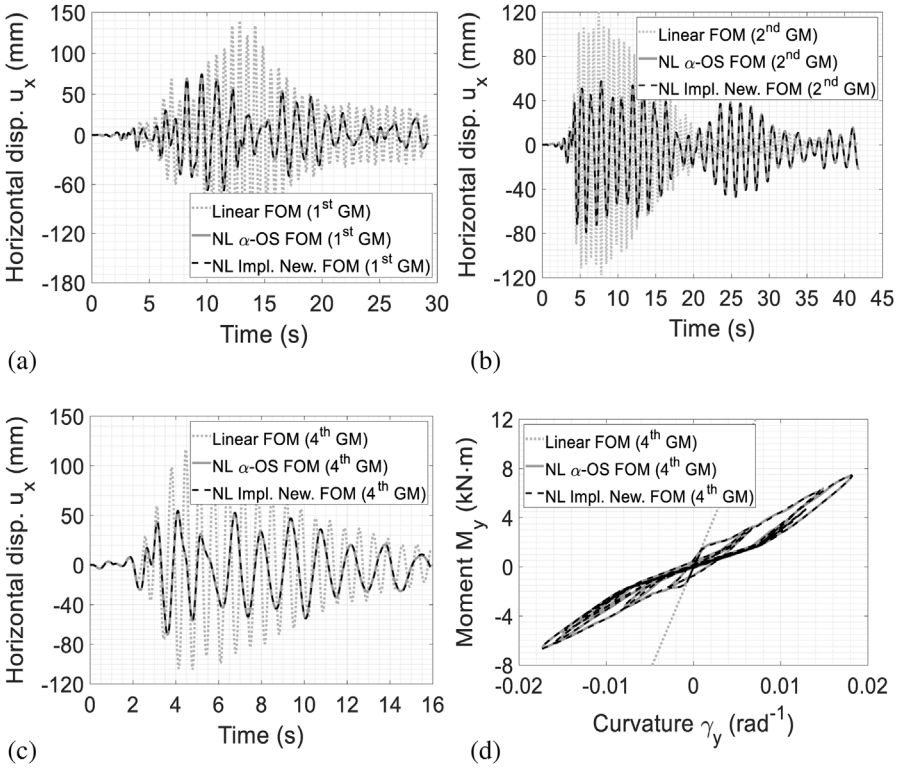

FIGURE 7 Displacement component u_x of the northwest corner—full-order model (FOM) with the 1st (a), 2nd (b), and 4th (c) ground motions, and moment/curvature response of the northwest corner with the 4th ground motion (d).

FOM responses to ground motions #1, #2, and #4. The FEM analyses were all performed with a time step Δt equal to 10 ms and an α parameter equal to -0.05 so that $\beta = 0.28$ and $\gamma = 0.55$ (Pegon & Pinto, 2000). All calculations were carried out on an Intel Core i9-10900K CPU @ 3.70 GHz and 64 GB RAM computer using MATLAB software. The memory usage remained constant and did not exceed 35% of the inherent memory of the computer.

The displacement component u_x of the northwest corner (see the location of the star in Figure 6a) is computed in Figure 7 for each ground motion using both the α-OS and the implicit Newmark methods (i.e., $\beta = 0.25$ and $\gamma = 0.50$). A relative tolerance of 10^{-6} was used to control the convergence of the implicit method. Both responses are quasi-identical despite being highly affected in amplitude and frequency by the material nonlinearities (see Figure 7d).

The CPU time and the error that are summarized in Table 3 quantify the applicability of the α-OS method to compute the nonlinear response to ground motions #1, #2, and #4.

In this paper, the solutions ($\boldsymbol{u}$, $\boldsymbol{r}$) are compared to the implicit Newmark reference ($\boldsymbol{u}^{\mathrm{FOM}}$, $\boldsymbol{r}^{\mathrm{FOM}}$) using the strain energy error $\varepsilon_{\mathrm{Ed}}$ defined in (15):

TABLE 3 Central processing unit (CPU) times and errors introduced by the α-operator splitting (α-OS) method for ground motions #1, #2, and #4.

Ground motion	$\varepsilon_{\mathrm{Ed}}$ (%)	CPU time: Impl. New. full-order model (FOM)	CPU time: α-OS FOM	Speed up factor (−)
# 1	0.17	1 h 34 min 58 s	11 min 28 s	8.2
# 2	0.08	1 h 51 min 28 s	14 min 12 s	7.8
# 4	0.09	53 min 14 s	6 min 47 s	7.8

$$\varepsilon_{\mathrm{E_d}} = \frac{\Delta E_{\mathrm{d}}}{E_{\mathrm{d}}^{\mathrm{FOM}}} \times 100\ \%$$
$$\Delta E_{\mathrm{d}} = \frac{1}{2N_t \Delta t} \int_0^{N_t \cdot \Delta t} \left| \Delta \boldsymbol{u}^{\mathrm{T}}(t)\, \Delta \boldsymbol{r}(t) \right| dt \tag{15}$$

where $E_{\mathrm{d}}^{\mathrm{FOM}}$ is the strain energy of the implicit Newmark FOM, ΔE_{d} is the difference in strain energy, N_t is the number of time intervals, Δt is the time step, $\Delta \boldsymbol{u} = \boldsymbol{u} - \boldsymbol{u}^{\mathrm{FOM}}$ is the difference in displacements, and $\Delta \boldsymbol{r} = \boldsymbol{r} - \boldsymbol{r}^{\mathrm{FOM}}$ is the difference in restoring forces. It should be noted that

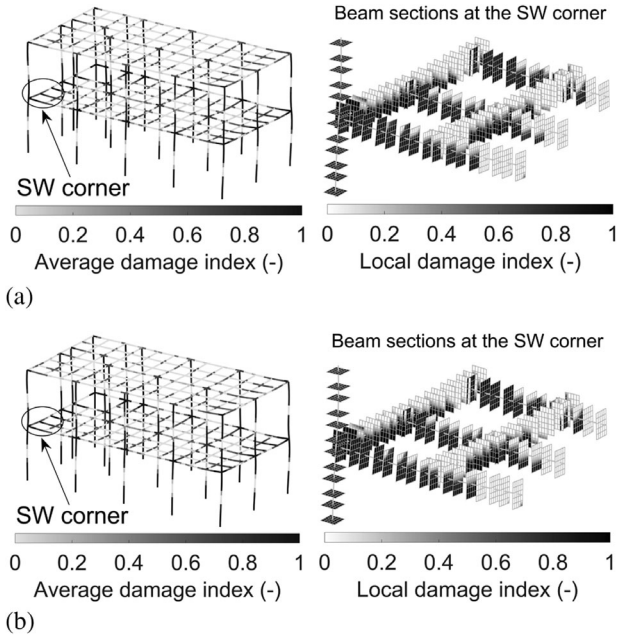

FIGURE 8 Damage index distribution applied to the final displacement field (amplification factor equal to 35) using ground motion #1: implicit Newmark method (a) and α-operator splitting (α-OS) method (b).

the dissipated energy could be used instead of the strain energy in (15) to quantify the ability of the solution to model the earthquake-induced degrading mechanisms. Its computation is not addressed in this paper but could be performed on the force/displacement responses using a rainflow method, which proved its efficiency for nonlinear fatigue-based structural health monitoring (Pavlou, 2022).

Table 3 shows that the strain energy error introduced by the α-OS method is almost negligible, with a value of less than 0.2%. In addition, the speed-up factor is approximately equal to 8 since no iteration or reassessment of the tangent stiffness matrix is required. Damage indices related to both methods are averaged on the beam elements and plotted in Figure 8 for ground motion #1. Local indices are also visible on beam sections located at the southwest corner of the building. The damage is quasi-identical at local and global scales regardless of the method used with 1268 damaged elements (see the darkened elements in Figure 8). This proves that the α-OS method is well suited for performing FEM analyses on models of RC structures that use softening damage laws, so it can advantageously be used with HROMs under the infinitesimal strains assumption.

4.5 | Truncation of the displacement and force bases

Dynamic responses computed using ground motions #1, #2, and #4 as external loadings were used to produce high-dimensional reference solutions. The displacement and force snapshots, which defined the training dataset, were then selected from the beginning to the end of each loading path-dependant solution from intervals of three-time steps (i.e., every 30 ms) to avoid unnecessary redundancy of the input data. Within the training dataset, 974 snapshots were related to ground motion #1, 1395 to #2, and 530 to #4. SVDs were then performed on two sets of displacement and force snapshots (i.e., $\boldsymbol{S}_{\mathrm{d}}$ and $\boldsymbol{S}_{\mathrm{f}}$, respectively) to build the POD and UDEIM modal bases $\boldsymbol{\Phi}$ and $\boldsymbol{\Psi}$ (see Figure 1). By considering a tolerance ε equal to 10^{-2} for the truncation of $\boldsymbol{\Phi}$, the criterion in (5) was fulfilled with a number n of 24 POD modes using the α-OS method and 22 POD modes using the implicit Newmark method (see Figure 9).

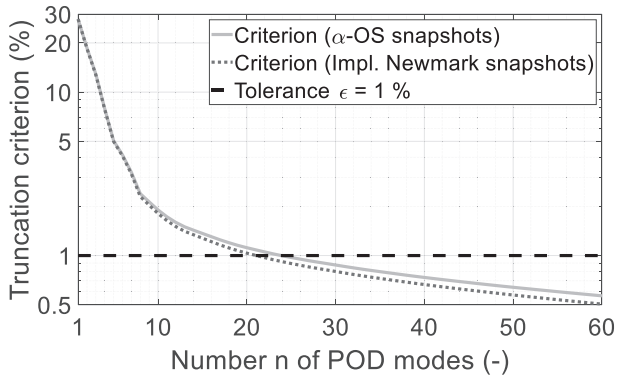

FIGURE 9 Criterion used to truncate the POD modal basis $\boldsymbol{\Phi}$.

TABLE 4 Error, online, and offline CPU times of the hyper-reduced order model (HROM) with several number of unassembled discrete empirical interpolation method (UDEIM) modes based on the response related to ground motion #5.

m (–)	Truncation criterion (%)	$\varepsilon_{\mathrm{Ed}}$ (%)	CPU time (s)	
			Offline	Online
50	9.37	143	32	42
100	5.66	2.43	33	20
150	3.90	0.54	35	26
200	2.86	0.35	37	35
250	2.18	0.21	40	42
300	1.70	0.27	43	47
350	1.34	0.16	47	71
400	1.07	0.14	52	79
450	0.87	0.14	58	82
500	0.70	0.15	64	96

Each HROM was then used to compute the response related to ground motion #5 using the α-OS method. The error, as well as the online and offline CPU times, is summarized in Table 4.

In addition, the displacement component u_x of the northwest corner is plotted for several HROMs in

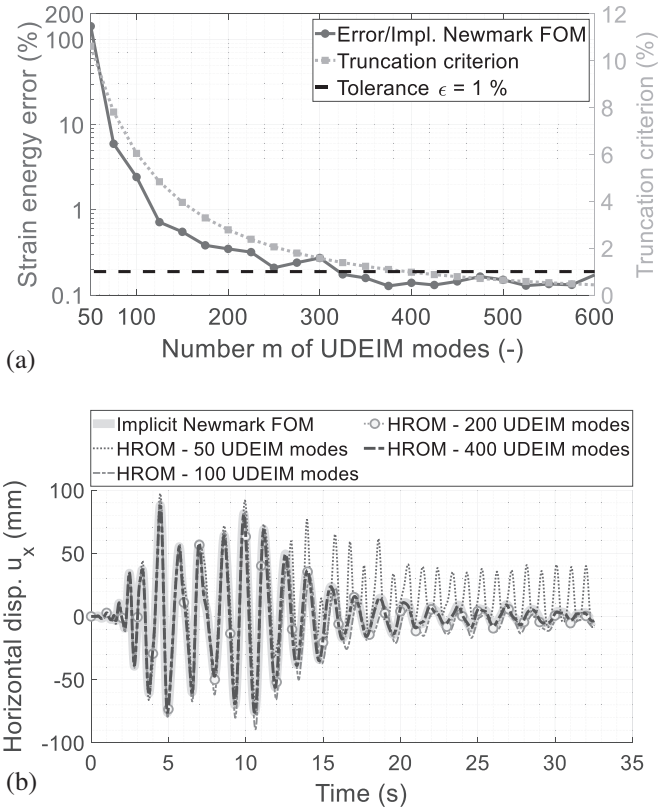

FIGURE 10 Strain energy error and truncation criterion with respect to the number m of UDEIM modes (a) and displacement component u_x of the northwest corner computed with ground motion #5 (24 POD modes) (b). HROM, hyper-reduced order model.

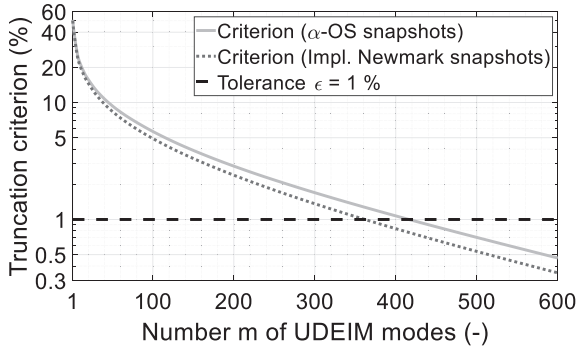

FIGURE 11 Criterion used to truncate the UDEIM modal basis $\boldsymbol{\Psi}$.

Figure 10b, while the strain energy error and the truncation criterion are drawn in Figure 10a with respect to the number m of UDEIM modes. Figure 10a highlights that the strain energy error does not necessarily decrease when new UDEIM modes are added as shown by the loss of accuracy with $m = 300$. Indeed, the loading path-dependency of the internal variables can lead to an additional error if the UDEIM approximation overestimates the components of the restoring force vector locally at some DOFs belonging to the RID. Such an error can occur, for example, when new UDEIM modes are added to $\boldsymbol{\Psi}$, even if the strain energy error stabilizes at a low value when enough UDEIM modes are taken into account.

The CPU times in Table 4 show that the duration of the offline phase, which includes the computation of the displacement basis $\boldsymbol{\Phi}$, the force basis $\boldsymbol{\Psi}$, the partition matrix $\boldsymbol{P}$, and the interpolation operator $\boldsymbol{A}$ (see Figure 1), is twice as high when the number m of UDEIM modes increases by a factor of 10. According to the DEIM procedure defined in Algorithm 1, the size of the matrix system to solve to find each new collocation component increases when a new UDEIM mode is added. As a result, the offline CPU time is higher since the value of m increases when the tolerance ε decreases. However, as the unused additional components of the RID are added a posteriori to the partition matrix $\boldsymbol{P}$, the size of the matrix system to solve when Algorithm 1 runs does not exceed $\mathbb{R}^{m \times m}$. Thus, the offline CPU time remains low since its value is less than 60 s when the minimal strain energy error $\varepsilon_{\text{Ed}} = 0.13\%$ is reached with ground motion #5 (see Figure 10a). The duration of the online phase also increases with respect to the number m of UDEIM modes since adding new collocation components increases the size of the RID. In comparison to an HROM made of 100 UDEIM modes, the online CPU time is five times higher when 500 UDEIM modes are taken into account, even if an insufficient number of modes may also lead to a higher CPU time, as it is the case when only 50 UDEIM modes are used (see Table 4). If the HROM is not accurate enough, the displacement and the strains are overestimated, increasing the time necessary to update the material properties on the RID.

The strain energy error ε_{Ed} plotted in Figure 10a is well stabilized when more than 400 UDEIM modes are used in the truncated basis $\boldsymbol{\Psi}$. Considering that the truncation criterion (5) is lower than 1.07% (see Table 4), a tolerance ε equal to 1% can thus be reasonably used to truncate $\boldsymbol{\Psi}$, which is the highest value that is usually recommended regardless of the physics of the case study. This choice leads to a basis made of 417 UDEIM modes using the α-OS method and 362 UDEIM modes using the implicit Newmark method (see Figure 11).

The value of m varies since an explicit prediction of the force snapshots is used with the α-OS method instead of the converged results. Thus, the data used to build the HROM are slightly different with the α-OS method, which explains why more UDEIM modes are required. Higher-dimensional bases $\boldsymbol{\Phi}$ and $\boldsymbol{\Psi}$ could also be required for irregular structures with more complex geometries since the singular values identified from the training dataset are expected to decrease more slowly, which could increase the

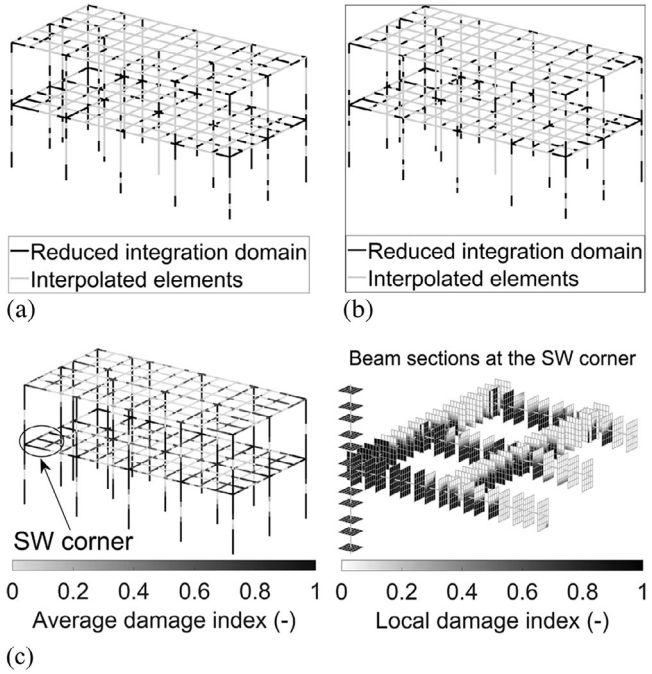

FIGURE 12 Reduced integration domains (RIDs) built using snapshots computed with the α-OS method (417 beam elements) (a) and the implicit Newmark method (362 beam elements) (b), and domain where nonlinearities are the most likely to appear according to the snapshots (1317 beam elements) (c).

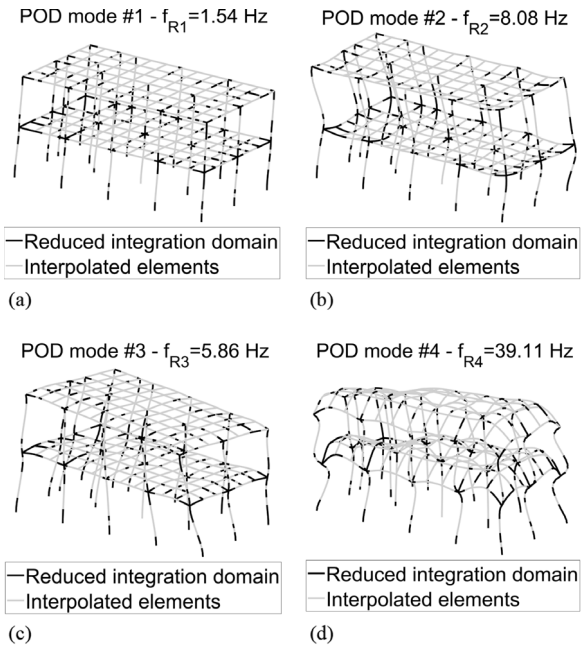

FIGURE 13 Shapes of POD mode #1 (a), POD mode #2 (b), POD mode #3 (c), and POD mode #4 (d) with snapshots computed using the α-OS method.

number of modes necessary to fulfill (5) using a tolerance of 1%.

The RIDs built using snapshots computed with the α-OS and implicit Newmark methods are drawn in Figure 12. When the α-OS method is used, the RID is made of 417 beam elements (see the black elements in Figure 12a). With the implicit Newmark method, the RID includes 362 beam elements (see Figure 12b). The number of elements in the RID is thus equal to m in both cases.

As shown by the maximal damage index distribution computed with ground motions #1, #2, and #4, damage may appear on 1317 beam elements (see Figure 12c). Thus, the RIDs are 68% and 73% smaller than the domain where nonlinearities are the most likely to appear, which saves a significant CPU time during the online phases.

The amplified shapes of the first four POD modes used to build the displacement basis $\boldsymbol{\Phi}$ are drawn in Figure 13, with snapshots computed using the α-OS method. The POD modes differ from the eigenmodes since they efficiently model local nonlinearities (e.g., damage) but depend on the loadings used to compute the nonlinear responses that are added to the training dataset. The frequency f_{Ri} that activates the ith POD mode $\boldsymbol{\varphi}_i \in \mathbb{R}^{N_{DOFs}}$ can be approximated using its Rayleigh quotient R_i (16):

$$f_{Ri} \approx \frac{\sqrt{R_i}}{2\pi} \quad \text{with} \quad R_i = \frac{\boldsymbol{\varphi}_i^{\mathrm{T}} \boldsymbol{K}_{\mathrm{E}} \boldsymbol{\varphi}_i}{\boldsymbol{\varphi}_i^{\mathrm{T}} \boldsymbol{M} \boldsymbol{\varphi}_i} \tag{16}$$

where $\boldsymbol{K}_{\mathrm{E}} \in \mathbb{R}^{N_{DOFs} \times N_{DOFs}}$ is the elastic stiffness matrix, and $\boldsymbol{M} \in \mathbb{R}^{N_{\mathrm{DOFs}} \times N_{\mathrm{DOFs}}}$ is the mass matrix.

POD mode #1 ($f_{R1} = 1.54$ Hz) is close to the eigenmode of bending #1 along the $\boldsymbol{x}$-axis ($f_1 = 1.47$ Hz). The shape of POD mode #2 ($f_{R2} \approx 8.0$ Hz) is close to the eigenmode of bending #2 along the $\boldsymbol{x}$-axis ($f_5 = 5.23$ Hz). POD mode #3 represents the torsional effects activated by the bidirectional horizontal loading and induced by the stairwell that increases the stiffness locally. The shape of POD mode #3 is close to the torsional eigenmode #1 about the $\boldsymbol{z}$-axis ($f_3 = 1.90$ Hz). POD mode #4 represents the bending strains due to the vertical loads (i.e., static dead and live loads, and vertical component of the ground motion). The frequencies provided by the Rayleigh quotients are higher than expected for POD modes #2 and #3 since floor deformations that refer to high-order eigenmodes are included in the POD modal shapes. The decrease of the truncation criterion in Figure 9 shows that POD modes #1, #2, and #3 contribute up to 72.0%, 9.5%, and 5.7% to the POD basis $\boldsymbol{\Phi}$, respectively. The response is thus mainly affected by bending using ground motions weighted by 1.0, −0.7, and 0.3 along the $\boldsymbol{x}$, $\boldsymbol{y}$, and $\boldsymbol{z}$-axes, respectively.

4.6 | Parametric analysis that involves several earthquakes

The HROMs built in Section 4.5 were used to compute the dynamic response of the two-story building (see Figure 6)

when subjected to ground motions #3, #5, #6, #7, #8, #9, #10, #11, and #12 (see Figure 4).

The earthquakes #1 to #12 define a parametric loading involving many variables (e.g., PGA, PGV, or average band-limited power) as explained in Section 4.3. But, since the evolution of natural ground motions is hard to describe on a reduced set of parameters, intervals cannot be explicitly identified for the parametric system. However, as the finite elements where damage grows (e.g., around the column/beam connections) are usually the same regardless the properties of the earthquake, hyper-reduction is expected to correctly approximate dynamic responses induced by random ground motions of the same order of magnitude.

The modeling assumptions (e.g., material properties, steel reinforcements, or areas of the sections) defined in Sections 4.1 and 4.2 remained the same for all the hyper-reduced simulations (i.e., online phases). The parametric analysis was repeated using the α-OS and the implicit Newmark methods to quantify the fidelity and the additional CPU time-saving allowed by the operator splitting when hyper-reduction is used.

Figure 14 compares the strain energy error, the online CPU times, and the number of iterations related to the FOMs, the POD ROMs, and the POD-UDEIM HROMs. The horizontal displacement of the northwest corner was also computed along the $\boldsymbol{x}$-axis using the implicit Newmark FOM and both HROMs (see Figure 15).

According to Figure 14a, the strain energy error is less than 0.7% for all the ground motions, which highlights the accuracy of the HROMs. The displacement component u_x of the Northwest corner computed using the HROMs also agrees well with the implicit Newmark FOM (see Figure 15j). For real-life applications, note that the error that is introduced by the hyper-reduction could also be quantified without knowing the response of the FOM using an error criterion based on the balance of the equation of motion in the high-dimensional basis as used by a priori ROM methods for selecting new modes (Chinesta et al., 2014).

Figure 14b shows that using an implicit Newmark method with a POD ROM leads to an online speed-up factor of 2. The POD method saves a significant part of the online CPU time with iterative methods (i.e., 50%) since the computational cost required to solve the matrix system is almost negligible. The POD-UDEIM is even more efficient, with a speed-up factor of 16. As less elements need to be updated when the online phase proceeds, approximately 94% of the online CPU time can thus be saved. Figure 14c demonstrates that twice as few iterations are required using reduced order models, which improves the efficiency of the POD and the POD-UDEIM even more.

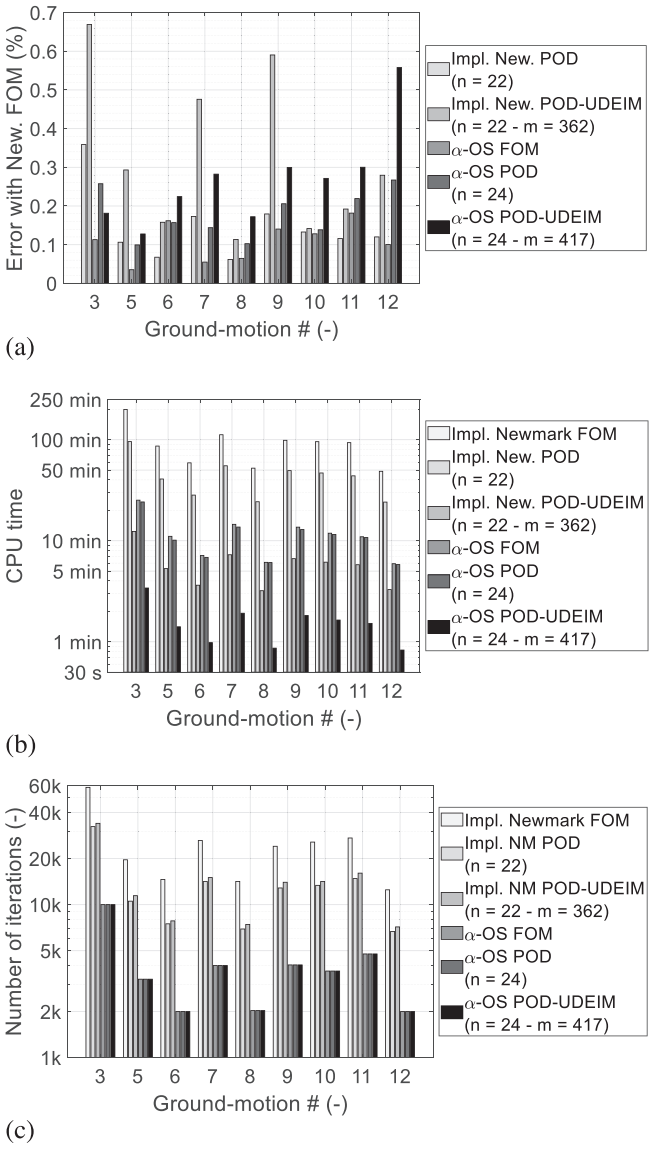

FIGURE 14 Strain energy error (a), online central processing unit (CPU) time (logarithmic scale) (b), and number of iterations (logarithmic scale) of the FOMs, POD ROMs, and POD-UDEIM HROMs.

Higher time-savings are reachable with the α-OS method as no reassessment of the tangent stiffness matrix or system inversion is required. Compared to the α-OS FOM, the online speed-up factor does not exceed 1.1 with the α-OS POD ROM but reaches 7.9 when the α-OS POD-UDEIM HROM is used (see Figure 14b). This value increases to become approximately equal to 60 if the α-OS HROM is compared to the implicit Newmark FOM.

The CPU times summarized in Table 5 quantify the duration of the parametric analysis, including the computation of the training data as well as the offline and online phases. The α-OS POD-UDEIM HROM saves a significant part of the CPU time since the response of

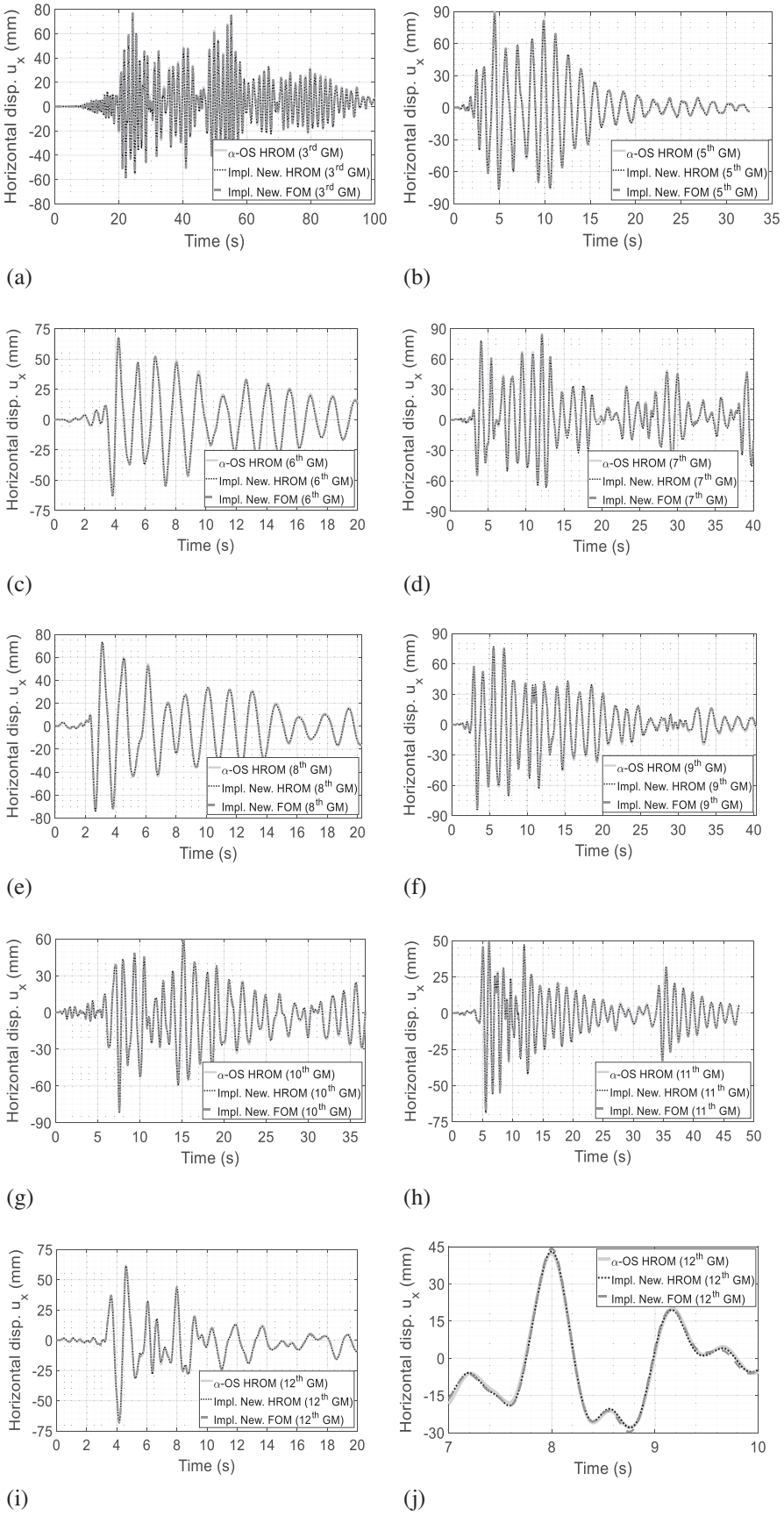

FIGURE 15 Displacement component u_x of the northwest corner related to ground motions #3 (a), #5 (b), #6 (c), #7 (d), #8 (e), #9 (f), #10 (g), #11 (h), #12 (i) and focus between 7 and 10 s with the 12th ground motion (j)—comparison between the FOM and the POD-UDEIM HROMs.

TABLE 5 Comparison of the CPU times necessary to achieve the parametric analysis involving several ground motions.

Method	CPU time
Implicit Newmark FOM	18 h 23 min 46 s
Implicit Newmark proper orthogonal decomposition–reduced order modeling (POD ROM)	11 h 7 min 13 s
Implicit Newmark POD-UDEIM HROM	5 h 13 min 3 s
α-OS FOM	2 h 18 min 50 s
α-OS POD ROM	2 h 14 min 27 s
α-OS POD-UDEIM HROM	47 min 44 s

the 12 ground motions is computed three times faster, compared to the α-OS FOM, and 23 times more quickly, compared to implicit Newmark FOM, which is the default method used by most industrial software. In addition, the POD-UDEIM is far more efficient than the POD method since the parametric analysis is achieved eight times faster when a UDEIM interpolation operator is used. Because the CPU time-saving of the entire analysis increases when the time necessary to compute the snapshots decreases, using HROMs with the α-OS method offers an excellent strategy to accelerate parametric analyses that involve several earthquakes. Section 4.7 proposes applying this methodology to another parametric analysis on the directionality of earthquakes.

4.7 | Parametric analysis on the directionality of earthquakes

An α-OS HROM was next used to compute the response related to ground motion #4 (see Figure 4d), assuming that the seismic waves may come from several directions. An angle θ was used as a parameter to define the orientation of the earthquake with respect to the $\boldsymbol{x}$-axis. The values of θ taken into account for the parametric analysis are drawn on the plan view of the mesh in Figure 16. The ground motion #4 was weighed by $\cos\theta$ in the x-direction, $\sin\theta$ in the y-direction, and 0.3 in the z-direction. θ was between 0 and 2π rad, and the response of the building was computed every $\pi/8$ rad.

To be sure that the HROM can correctly model bending and torsion at floor level, snapshots were built with $\theta = 0$ rad (i.e., bending along the longitudinal axis), $\theta = \pi/4$ rad (i.e., torsion around the vertical axis), and $\theta = \pi/2$ rad (i.e., bending along the transversal axis) using the α-OS method (see the bold axes in Figure 16). Because training data are less redundant when the weights applied to the ground motion vary, the snapshots were selected every 10 ms. All the 4770 available snapshots (i.e., 1590 per training FEM analysis) were then used to build the HROM.

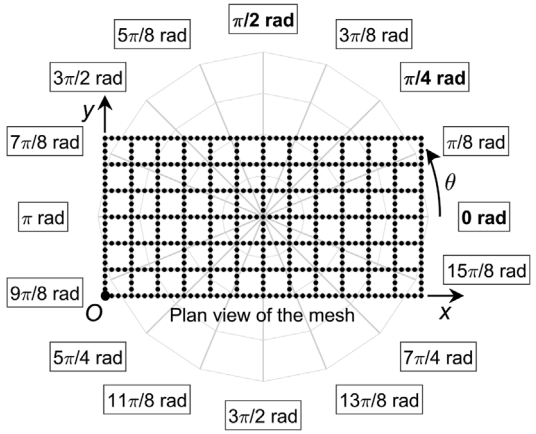

FIGURE 16 Orientations of the seismic waves used in the parametric analysis focusing on the directionality of earthquakes (plan view of the mesh).

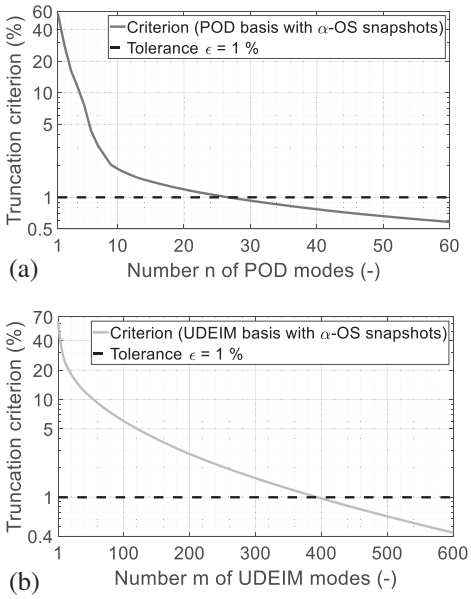

FIGURE 17 Criteria used to truncate the POD (a) and UDEIM (b) modal bases $\boldsymbol{\Phi}$ and $\boldsymbol{\Psi}$.

Considering a truncation criterion ε equal to 1% led to a displacement basis $\boldsymbol{\Phi}$ made of 27 POD modes (see Figure 17a) and a force basis $\boldsymbol{\Psi}$ made of 395 UDEIM modes (see Figure 17b). It should be noted that approximately 80 s were required to build the HROM (i.e., offline CPU time), including the displacement basis $\boldsymbol{\Phi}$ (i.e., 20 s) and the interpolation operator $\boldsymbol{A}$ (i.e., 60 s). As a result, the duration of the offline phase remained low, compared to the time necessary to compute the snapshots (i.e., 15 min).

The damage index distribution and the first POD modes defined using the training data are shown in Figure 18. According to the snapshots, damage may appear on 1299 elements (see the darkened lines in Figure 18a). The RID

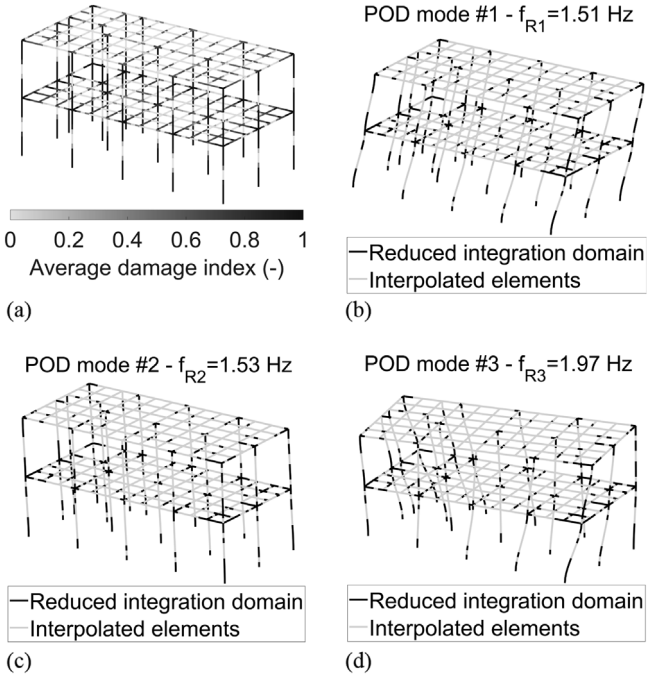

FIGURE 18 Domain where damage may appear (1299 beam elements) (a) and shapes of POD mode #1 (b), POD mode #2 (c), and POD mode #3 (d) drawn with the RID (395 beam elements).

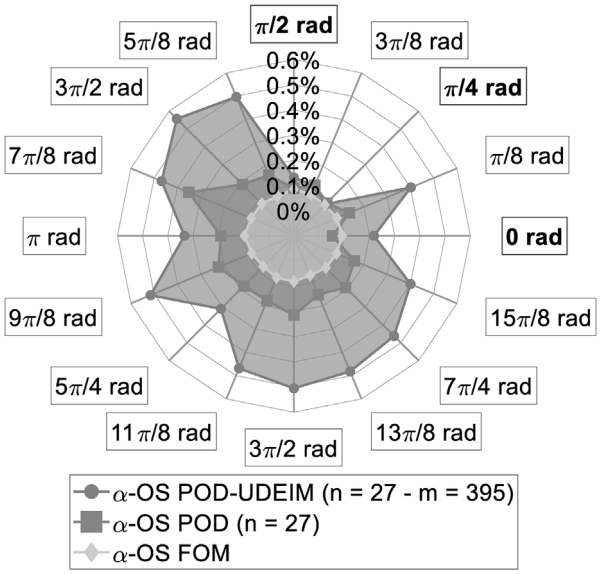

FIGURE 19 Strain energy error of the α-OS FOM, POD ROM, and POD-UDEIM HROM ($n = 27 - m = 395$) for each value of θ.

TABLE 6 CPU time of the α-OS FOM, POD ROM, and POD-UDEIM HROM ($n = 27 - m = 395$) for each value of θ.

θ (rad)	CPU time Impl. New.	α-OS FOM	α-OS POD	α-OS HROM
$\pi/8$	48 min 5 s	5 min 21 s	5 min 18 s	43 s
$3\pi/8$	52 min 58 s	5 min 18 s	5 min 21 s	43 s
$5\pi/8$	50 min 9 s	5 min 3 s	4 min 56 s	41 s
$3\pi/2$	49 min 32 s	5 min 7 s	4 min 58 s	42 s
$7\pi/8$	47 min 15 s	4 min 41 s	4 min 36 s	39 s
π	43 min 3 s	4 min 24 s	4 min 18 s	36 s
$9\pi/8$	50 min 38 s	5 min 10 s	5 min 10 s	44 s
$5\pi/4$	53 min 3 s	5 min 32 s	5 min 31 s	47 s
$11\pi/8$	51 min 24 s	5 min 16 s	5 min 13 s	44 s
$3\pi/2$	54 min 44 s	4 min 51 s	4 min 40 s	39 s
$13\pi/8$	47 min 58 s	5 min 0 s	4 min 50 s	41 s
$7\pi/4$	52 min 7 s	5 min 9 s	4 min 57 s	42 s
$15\pi/8$	44 min 29 s	4 min 42 s	4 min 30 s	38 s

is made of 395 elements and is approximately 70% smaller (see the black lines in Figure 18b–d). POD mode #1 is close to the eigenmode of bending #1 along the $\boldsymbol{y}$-axis ($f_{R1} \approx f_1 = 1.41$ Hz), #2 to the eigenmode of bending #1 along the $\boldsymbol{x}$-axis ($f_{R2} \approx f_2 = 1.47$ Hz), and #3 to the torsional eigenmode #1 about the $\boldsymbol{z}$-axis ($f_{R3} \approx f_3 = 1.90$ Hz). According to Figure 17a, POD modes #1, #2, and #3 are all significant since they contribute up to 42.7%, 28.9%, and 12.3% to $\boldsymbol{\Phi}$, respectively. As expected by the choice of the training data, the POD modal basis can thus correctly describe torsion and bending at floor level.

The strain energy errors and the online CPU times related to the α-OS FOM, the α-OS POD ROM, and the α-OS POD-UDEIM HROM are summarized in Figure 19 and Table 6, respectively. Figure 19 shows that the strain energy error ε_{Ed} does not exceed 0.35% with the POD ROM, while its value is between 0.11% ($\theta = 3\pi/8$ rad) and 0.56% ($\theta = 3\pi/2$ rad) with the POD-UDEIM HROM. With an error of less than 1%, the HROM can thus correctly describe the nonlinear behavior of the damageable structure.

The CPU times in Table 6 show that even if all FEM analyses are performed using the same ground motion, their duration varies from 43 min ($\theta = \pi$) to 55 min ($\theta = 3\pi/2$ rad). The values of θ that best activate torsional effects at floor level (e.g., $\theta = 7\pi/4$ rad) or bending movements about the weak axis (e.g., $\theta = 3\pi/2$ rad) usually lead to more significant damage, which increases the CPU time since more iterations are required to update the material properties locally. The online CPU times are approximately 10 times lower with the α-OS FOM (i.e., 303 s) as well as with the α-OS POD ROM (i.e., 298 s), and 72 times lower with the α-OS POD-UDEIM HROM (i.e., 41 s).

Let $u_\theta = u_x \cdot \cos\theta + u_y \cdot \sin\theta$ be the horizontal displacement of the northwest corner along the direction of earthquake #4, computed in Figure 20 for the eight values of θ related to the highest strain energy error. The α-OS HROM agrees well with the implicit Newmark FOM since the amplitude and the frequency of both responses are almost the same. However, slight amplitude variations may appear when the displacement reaches extrema (e.g., after

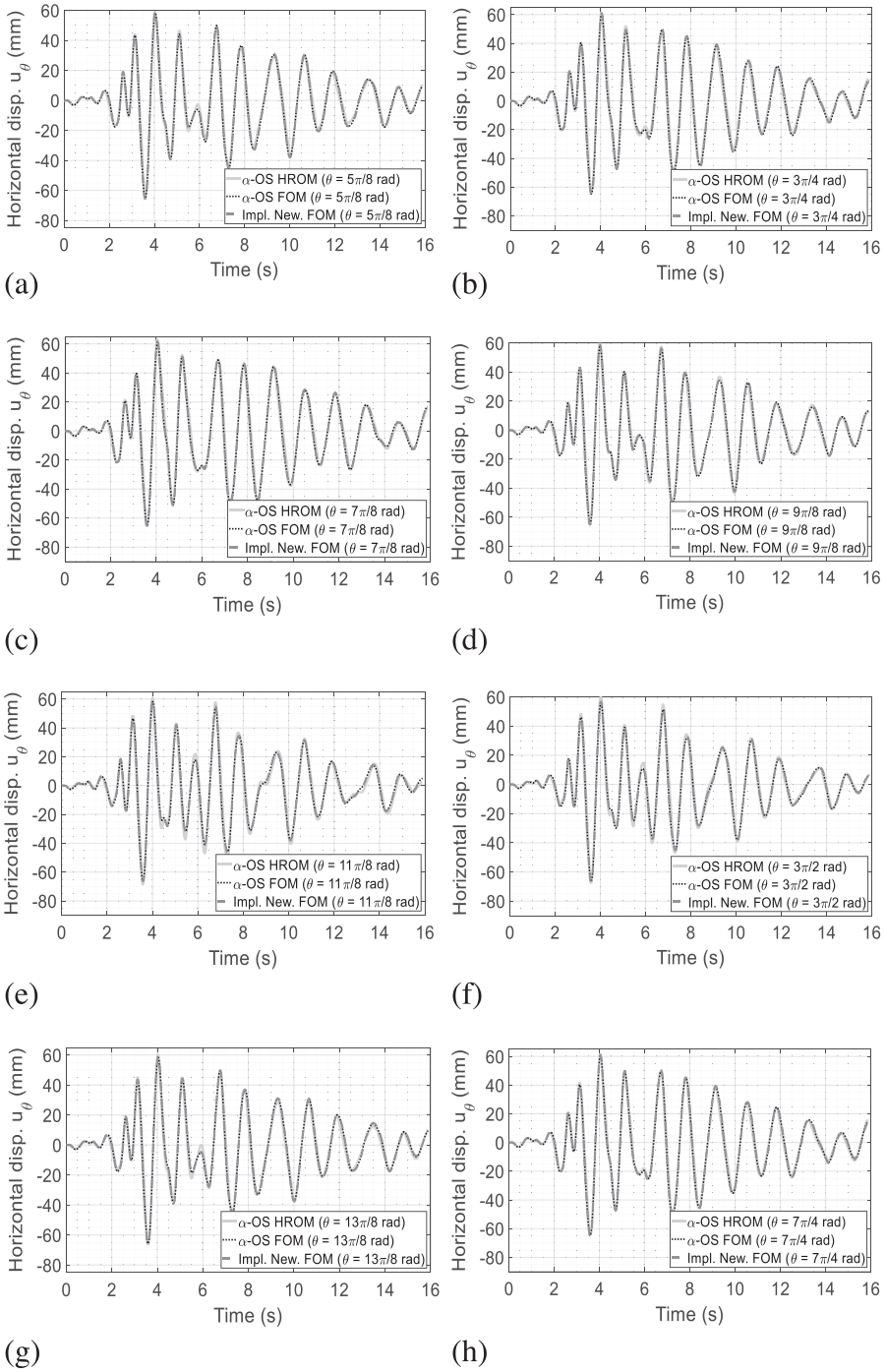

FIGURE 20 Displacement u_θ of the northwest corner along the direction of the earthquake with θ equal to $5\pi/8$ rad (a), $3\pi/4$ rad (b), $7\pi/8$ rad (c), $9\pi/8$ rad (d), $11\pi/8$ rad (e), $3\pi/2$ rad (f), $13\pi/8$ rad (g), and $7\pi/4$ rad (h)—comparison between the FOMs and the POD-UDEIM HROM.

6 s with $\theta = 11\pi/8$ rad, see Figure 20e). Although the accuracy of HROMs is high enough for earthquake engineering purposes, this approach appears to be more limited when the direction of the ground motion is used as a parameter.

Table 7 summarizes the CPU times necessary to achieve the parametric analysis, including the computation of training data as well as the offline and online phases. The calculations can be performed in 25 min 30 s using the

TABLE 7 Comparison of the CPU times necessary to achieve the parametric analysis on the directionality of earthquakes.

Method	CPU time
Implicit Newmark FOM	13 h 14 min 10 s
α-OS FOM	1 h 20 min 43 s
α-OS POD ROM	1 h 19 min 49 s
α-OS POD-UDEIM HROM	25 min 27 s

α-OS HROM, including 15 min to compute three sets of snapshots (i.e., 59%), 1 min 20 s to build the HROM (i.e., offline phase, 5%), and 9 min to perform 13 online FEM analyses (i.e., 36%). The computation of snapshots is a significant part of the hyper-reduction procedure because the training data need to be assessed on a full basis, even if the α-OS method is used. However, using an HROM is still helpful since the CPU time is approximately 3.2 times lower, compared to the α-OS FOM, and 31 times lower, compared to the implicit Newmark FOM. The computational cost related to the parametric analysis on θ is thus highly reduced, showing that α-OS HROMs are well suited to accelerate parametric analyses on the directionality of earthquakes.

5 | CONCLUSION

This paper used a hyper-reduction procedure to accelerate nonlinear dynamic parametric analyses on a civil engineering structure. A POD reduction using a UDEIM to approximate the restoring forces was combined with a non-iterative α-OS time integration to reduce as much as possible the calculation times. An asymmetric two-story RC building subjected to earthquakes, which was modeled using multi-fiber beam elements, has been used as a case study. Complex dissipative mechanisms were introduced locally using a quasi-brittle damage law with softening and frictional sliding for the concrete, while a bilinear elastic–plastic law with kinematic hardening was used for the steel. Applications to analyses that used variable ground motions or several orientations for the earthquake demonstrated the efficiency of the proposed approach since

1. using a non-iterative α-OS method accelerated eight times the computation of full order solutions with a negligible error;
2. hyper-reduced solutions were quasi-identical to the full-order references, with an error of less than 0.6%;
3. hyper-reduction accelerated eight times the computation of the restoring forces when iterating;
4. implicit methods converged more easily with hyper-reduction since two times less iterations were required;
5. using an α-OS method with hyper-reduction accelerated more than 60 times the computation of new structural responses, compared to the implicit FOM.

Guidelines for performing seismic analyses were identified according to these results, which showed that

1. a tolerance of 1% can reasonably be used in (5) for the truncation of the displacement and force bases;
2. HROMs of structures can be designed to simulate earthquake databases using a training dataset that mixes responses of very high and moderate intensities;
3. HROMs adaptable to various loading directions can be built mixing training data computed with earthquake oriented along the longitudinal, transversal, and 45° axes.

Using hyper-reduction with a non-iterative α-OS method proved efficient in accelerating parametric analyses with variable loading properties (e.g., frequency, PGA, strong motion phase duration, or orientation of ground motions) on a model that introduced complex nonlinear dissipative mechanisms. Such a method could advantageously be used to build parametric response surfaces for damageable structures coupling training data computed from nonlinear dynamic FEM analyses with values interpolated using machine learning or kriging algorithms. Parametric analyses involving earthquakes of differing orders of magnitude (e.g., fragility curves), other finite elements (e.g., multilayer plates), or variable mechanical properties (e.g., tensile strength) could also be performed using hyper-reduction.

ORCID

Fabrice Gatuingt https://orcid.org/0000-0002-9185-4719

REFERENCES

Adeli, H., Gere, J., & Weaver, W. Jr. (1978). Algorithms for nonlinear dynamics. *Journal of Structural Engineering, ASCE*, *104*(ST2), 263–280.

Adeli, H., & Yu, G. (1995). An integrated computing environment for solution of complex engineering problems using the object-oriented programming paradigm and a blackboard architecture. *Computers and Structures*, *54*(2), 255–0265.

Alcocer, S., Behrouzi, A., Brena, S., Elwood, K. J., Irfanoglu, A., Kreger, M., Lequesne, R., Mosqueda, G., Pujol, S., Puranam, A., Rodriguez, M., Shah, P., Stavridis, A., & Wood, R. (2020). Observations about the seismic response of RC buildings in Mexico City. *Earthquake Spectra*, *36*, 154–174.

Antil, H., Heinkenschloss, M., & Sorensen, D. C. (2014). Application of the discrete empirical interpolation method to reduced order modeling of nonlinear and parametric systems. In A. Quarteroni, & G. Rozza (Eds.), *Reduced order methods for modeling and computational reduction*. MS&A - Modeling, Simulation and Applications, vol 9, (pp. 101–136). Springer, Cham.

Astrid, P. (2004). *Reduction of process simulation models: A proper orthogonal decomposition approach*. (Doctoral dissertation, Technische Universiteit Eindhoven).

Ayoub, N., Deü, J.-F., Larbi, W., Pais, J., & Rouleau, L. (2022). Application of the POD method to nonlinear dynamic analysis of reinforced concrete frame structures subjected to earthquakes. *Engineering Structures*, *270*, 114854.

Azeez, M. F. A., & Vakakis, A. F. (1999). Numerical and experimental analysis of a continuous overhung rotor undergoing

vibro-impacts. *International Journal of Non-Linear Mechanics*, *34*(3), 415–435.

Benner, P., Gugercin, S., & Willcox, K. (2015). A survey of projection-based model reduction methods for parametric dynamical systems. *SIAM Review*, *57*(4), 483–531.

Bui-Thanh, T., Damodaran, M., & Willcox, K. (2003). Proper orthogonal decomposition extensions for parametric applications in compressible aerodynamics. *21st Applied Aerodynamics Conference, AIAA Paper 4213*, Orlando, FL.

Chambreuil, C. (2022). *Modelling of damping in nonlinear dynamic analyses of reinforced concrete structures: Constitutive formulations and experimental identification*. (Doctoral dissertation, ENS Paris-Saclay).

Chaturantabut, S., & Sorensen, D. C. (2010). Nonlinear model reduction via discrete empirical interpolation. *SIAM Journal on Scientific Computing*, *32*(5), 2737–2764.

Chinesta, F., Keunings, R., & Leygue, A. (2014). *The proper generalized decomposition for advanced numerical simulations*. Springer International Publishing.

Chopra, A. K. (2017). *Dynamics of structures: Theory and applications to earthquake engineering* (5th ed.). Pearson.

Combescure, D., Pegon, P., & Magonette, G. (1995). Numerical investigation of the impact of experimental errors on various pseudo-dynamic integration algorithms. In G. Duma (Ed.), *Proceedings of the 10th European conference on earthquake engineering* (pp. 2479–2484). Balkema.

Craig, R. R., & Bampton, M. C. (1968). Coupling of substructures for dynamic analyses. *AIAA Journal*, *6*(7), 1313–1319.

Davenne, L., Ragueneau, F., Mazars, J., & Ibrahimbegovic, A. (2003). Efficient approaches to finite element analysis in earthquake engineering. *Computers and Structures*, *81*, 1223–1239.

De Boe, P., & Golinval, J.-C. (2003). Principal component analysis of a piezosensor array for damage localization. *Structural Health Monitoring*, *2*(2), 137–144.

Diana, L., Manno, A., Lestuzzi, P., Podestà, S., & Luchini, C. (2018). Impact on displacement demand reliability for seismic vulnerability assessment at an urban scale. *Soil Dynamics and Earthquake Engineering*, *112*, 35–52.

Drmac, Z., & Gugercin, S. (2016). A new selection operator for the discrete empirical interpolation method—Improved a priori error bound and extensions. *SIAM Journal on Scientific Computing*, *38*(2), A631–A634.

Epureanu, B. (2003). A parametric analysis of reduced order models of viscous flows in turbomachinery. *Journal of Fluids and Structures*, *17*(7), 971–982.

Everson, R., & Sirovich, L. (1995). Karhunen-Loève procedure for gappy data. *Journal of the Optical Society of America A*, *12*(8), 1657–1664.

Ghavamian, F., Tiso, P., & Simone, A. (2017). POD-DEIM model order reduction for strain-softening viscoplasticity. *Computer Methods in Applied Mechanics and Engineering*, *317*, 458–479.

Guyan, R. J. (1965). Reduction of stiffness and mass matrices. *AIAA Journal*, *3*(2), 380–380.

Hafezolghorani, M., Hejazi, F., Jaafar, M. S., & Adeli, H. (2022). Plasticity model for partially prestressed concrete frame elements. *Structures*, *38*, 630–651.

Hall, K. C., Thomas, J. P., & Dowell, E. H. (2000). Proper orthogonal decomposition technique for transonic unsteady aerodynamic flows. *AIAA Journal*, *38*(10), 1853–1862.

Hemez, F. M., & Doebling, S. W. (2001). Review and assessment of model updating for non-linear, transient dynamics. *Mechanical Systems and Signal Processing*, *15*(1), 45–74.

Hervé-Secourgeon, G., Hervé-Secourgeon, E., Bottoni, M., Voldoire, F., Razafimbelo, M., Gatuingt, F., Oliver-Leblond, C., Honorio, T., Kamesh, A., Habib, S., & Escoffier, F. (2021). On structural finite element modeling strategies and their influence on the optimization of final constructability of reinforced concrete structures. *Nuclear Engineering and Design*, *385*, 111541.

Hilber, H., Hugues, T., & Taylor, R. (1977). Improved numerical dissipation for time integration algorithms in structural dynamics, *Earthquake Engineering and Structural Dynamics*, *5*(3), 283–292.

Hou, T., Meerbergen, K., Roels, S., & Janssen, H. (2020). POD-DEIM model order reduction for nonlinear heat and moisture transfer in building materials. *Journal of Building Performance Simulation*, *13*(6), 645–661.

Hwang, J.-S., Kwon, D. K., & Kareem, A. (2022). A modal-based Kalman filtering framework for mode extraction and decomposition of damped structures. *Computer-Aided Civil and Infrastructure Engineering*, *38*, 1274–1289.

Karhunen, K. (1946). Über lineare Methoden in der Wahrscheinlichkeitsrechnung. *Annals of Academic Science Fennicae, Series A1 Mathematics and Physics*, *37*, 3–79.

Kosambi, D. D. (1943). Statistics in function space. *Journal of Indian Mathematical Society*, *7*, 76–88.

Lai, Q., Hu, J., Xu, L., Xie, L., & Lin, S. (2022). Method for ranking pulse-like ground motions according to damage potential for reinforced concrete frame structures. *Buildings*, *12*, 754.

Loève, M. (1945). Analyse harmonique générale d une fonction aléatoire. *Comptes Rendus de l'Académie des Sciences*, *220*, 380–382.

Maierhofer, J., & Rixen, D. J. (2022). Model order reduction using hyperreduction methods (DEIM, ECSW) for magnetodynamic FEM problems. *Finite Elements in Analysis and Design*, *209*, 103793.

Nakashima, M., Kato, H., & Takaoka, E. (1992). Development of real-time pseudo dynamic testing. *Earthquake Engineering and Structural Dynamics*, *21*(1), 79–92.

Noureldin, M., Abuhmed, T., Saygi, M., & Kim, J. (2023). Explainable probabilistic deep learning framework for seismic assessment of structures using distribution-free prediction intervals. *Computer-Aided Civil and Infrastructure Engineering*, *38*, 1677–1698.

Ozdagli, A. I., & Koutsoukos, X. (2019). Machine learning based novelty detection using modal analysis. *Computer-Aided Civil and Infrastructure Engineering*, *34*, 1119–1140.

Pantò, B., Caddemi, S., Caliò, I., & Spacone, E. (2021). A 2D beam-column joint macro-element for the nonlinear analysis of RC frames. *Earthquake Engineering and Structural Dynamics*, *50*, 935–954.

Pavlou, D. (2022). A deterministic algorithm for nonlinear, fatigue-based structural health monitoring. *Computer-Aided Civil and Infrastructure Engineering*, *37*, 809–831.

Pegon, P., & Pinto, V. (2000). Pseudo-dynamic testing with substructuring at the ELSA Laboratory. *Earthquake Engineering and Structural Dynamics*, *29*, 905–925.

Peherstorfer, B., Butnaru, D., Willcox, K., & Bungartz, H.-J. (2014). Localized discrete empirical interpolation method. *SIAM Journal on Scientific Computing*, *36*(1), A168–A192.

Radermacher, A., & Reese, S. (2016). POD-based model reduction with empirical interpolation applied to nonlinear elasticity. *International Journal for Numerical Methods in Engineering*, *107*(6), 425–448.

Ravindran, S. S. (2000). A reduced-order approach for optimal control of fluids using proper orthogonal decomposition. *International Journal for Numerical Methods in Fluids*, *34*(5), 425–448.

Rayleigh, B. (1896). *The theory of sound* (Vol. 2). Macmillan.

Richard, B., & Ragueneau, F. (2013). Continuum damage mechanics based model for quasi brittle materials subjected to cyclic loadings: Formulations, numerical implementation and applications. *Engineering Fracture Mechanics*, *98*, 383–406.

Roy, A., & Nabi, M. (2021). Modeling of MEMS electrothermal microgripper employing POD-DEIM and POD method. *Microelectronics Reliability*, *125*, 114338.

Rutzmoser, J. B. (2017). *Model order reduction for nonlinear structural dynamics: Simulation-free approaches*. (Doctoral dissertation, Technischen Universität München).

Sarma, K., & Adeli, H. (1998). Cost optimization of concrete structures. *Journal of Structural Engineering, ASCE*, *124*(5), 570–578.

Sirovich, L. (1987). Turbulence and the dynamics of coherent structures. I. Coherent structures. *Quarterly of Applied Mathematics*, *45*(3), 561–571.

Stoter, S. K. F., Jessen, E., Niedens, V., & Schillinger, D. (2022). A DEIM driven reduced basis method for the diffuse Stokes/Darcy model coupled at parametric phase-field interfaces. *Computational Geosciences*, *26*, 1465–1502.

Terrien, M. (1980). Emission acoustique et comportement mécanique post-critique d'un béton sollicité en traction. *Bulletin de Liaison Labo. Ponts et Chaussées*, *105*, 65–72.

Tiso, P., & Rixen, D. J. (2013). Discrete empirical interpolation method for finite element structural dynamics. *Nonlinear Modelling and Applications*, *2*, 53–65.

Wen, W., Hu, J., Zhai, C., & Pei, S. (2023). Explainable probabilistic deep learning framework for seismic assessment of structures using distribution-free prediction intervals. *Computer-Aided Civil and Infrastructure Engineering*, *38*(12), 1677–1698.

Willcox, K. (2006). Unsteady flow sensing and estimation via the gappy proper orthogonal decomposition. *Computers & Fluids*, *35*(2), 208–226.

Xu, J., Spencer, B. F., Lu, X., Chen, X., & Lu, L. (2017). Optimization of structures subject to stochastic dynamic loading. *Computer-Aided Civil and Infrastructure Engineering*, *32*, 657–673.

Yu, G., & Adeli, H. (1993). Objet-oriented finite element analysis using EER model. *Journal of Structural Engineering, ASCE*, *119*(9), 2763–2781.

Yuan, Y., Au, F. T. K., Yang, D., & Zhang, J. (2023). Active learning structural model updating of a multisensory system based on Kriging method and Bayesian inference. *Computer-Aided Civil and Infrastructure Engineering*, *32*, 657–673.

How to cite this article: Bodnar, B., Larbi, W., Titirla, M., Deü, J.-F., Gatuingt, F., & Ragueneau, F. (2024). Hyper-reduced order models for accelerating parametric analyses on reinforced concrete structures subjected to earthquakes. *Computer-Aided Civil and Infrastructure Engineering*, *39,* 476–497. https://doi.org/10.1111/mice.13120